

THE AQUARIUS CO-MOVING GROUP IS NOT A DISRUPTED CLASSICAL GLOBULAR CLUSTER¹

ANDREW R. CASEY^{2,3}, STEFAN KELLER², ALAN ALVES-BRITO^{2,4}, ANNA FREBEL³, GARY DA COSTA², AMANDA KARAKAS², DAVID YONG², KEVIN SCHLAUFMAN³, HEATHER R. JACOBSON³, QINSI YU³, CHERIE FISHLOCK²

Draft version August 9, 2013

ABSTRACT

We present a detailed analysis of high S/N , high-resolution spectra for 5 Aquarius stream stars observed with the MIKE spectrograph on the Magellan Clay telescope. Our sample represents one third of the 15 members in the stream. We find the stream is not mono-metallic; the metallicity ranges from $[Fe/H] = -0.63$ to -1.58 dex. No anti-correlation in Na-O abundances is present, and we find a strong positive Mg-Al relationship, similar to that observed in the thick disc. We find no evidence that the stream is a result of a disrupted classical globular cluster, contrary to a previously published claim. High $[(Na, Ni, \alpha)/Fe]$ and low $[Ba/Y]$ abundance ratios in the stream suggests it is not a tidal tail from a disrupted dwarf galaxy, either. The stream is chemically indistinguishable from Milky Way field stars with the exception of one candidate, C222531-145437. From its position, velocity, and detailed chemical abundances, C222531-145437 is likely a star that was tidally disrupted from ω -Centauri. We propose the Aquarius stream is galactic in origin, and could be the result from a disc-satellite perturbation in the Milky Way thick disc on the order of a few gigayear ago. Derived orbits, UVW velocities, and angular momenta of the Aquarius members offer qualitative support for our hypothesis. Assuming C222531-145437 is a tidally disrupted member of ω -Centauri, this system is the most likely disc perturber. In the absence of compelling chemical and/or dynamical evidence that the Aquarius stream is the tidal tail of a disrupted satellite, we advocate the “Aquarius group” as a more appropriate description. Like the Canis Major over-density, as well as the Hercules and Monoceros groups, the Aquarius group adds to the list of kinematically-identified substructures that are not actually accreted material; they are simply part of the rich complexity of the Milky Way structure.

Keywords: Galaxy: halo, structure

1. INTRODUCTION

Galaxies are formed hierarchically through chaotic mergers of smaller systems, and the Milky Way is no exception (Bullock & Johnston 2005; Helmi 2008). The accumulating stellar debris in our own Galactic halo provides ongoing evidence for such merging events (e.g. Bell et al. 2008). As satellites fall towards the Galaxy, tidal forces disrupt the system, hurtling stars in leading and trailing directions. The position and velocities of stars within these “stellar streams” are sensitive to the Galactic potential. As such, their phase-space information can collectively constrain the fraction and distribution of accreted matter in the galaxy, the sub-halo mass function, as well as the shape and extent of the Milky Way’s dark matter halo. Additionally, individual chemical abundances can trace the chemical evolution of the Galaxy and its satellite systems.

Wide-field deep imaging surveys have proved excellent sources for finding stellar streams (e.g. Belokurov et al. 2007). Dozens of streams have been identified

through careful photometric selections and matched-filtering techniques, with some to a galactocentric distance of 100 kpc (e.g., see Drake et al. 2013). Indeed, it is clear that a large fraction of the stellar halo has been built up by accretion. However, as Helmi & White (1999) point out, these detection strategies are most successful for identifying streams that are sufficiently distant from the solar neighbourhood. A nearby stream, within ~ 10 kpc, will not appear as a photometric over-density because the stars would be sparsely positioned across the sky. Such substructures would only be detectable by their kinematics, or perhaps with precise elemental abundances through a “chemical tagging” approach (e.g. see Freeman & Bland-Hawthorn 2002). The confirmation of such substructures would serve to substantially increase the fraction of the known accreted material in the Galaxy.

It is therefore necessary to spectroscopically survey stars in the solar neighbourhood to reveal any nearby substructures. The Radial Velocity Experiment (RAVE) team began such a survey in 2003 and has taken spectra of over 500,000 stars across $17,000$ deg² (Steinmetz et al. 2006). The primary goal of RAVE is to obtain radial velocities for stars in the solar neighbourhood and beyond. In an attempt to remain kinematically unbiased, RAVE candidates were selected solely by their apparent magnitude ($9 < I < 13$). Almost all of these candidates have published radial velocities (Steinmetz et al. 2006), and for a subset of stars with a sufficient signal-to-noise (S/N) ratio, stellar parameters have been derived by a

¹ This paper includes data gathered with the 6.5 meter Magellan Telescopes located at Las Campanas Observatory, Chile.

² Research School of Astronomy and Astrophysics, Australian National University, Canberra, ACT 2611, Australia; acasey@mso.anu.edu.au

³ Massachusetts Institute of Technology, Kavli Institute for Astrophysics and Space Research, 77 Massachusetts Avenue, Cambridge, MA 02139, USA

⁴ Departamento de Astronomía y Astrofísica, Pontificia Universidad Católica de Chile, Av. Vicuña Mackenna 4860, Macul, 782-0436 Santiago, Chile

χ^2 -minimisation technique (Zwitter et al. 2008; Siebert et al. 2011).

Using these data, Williams et al. (2011) identified a co-moving group of nearby ($0.5 \text{ kpc} \lesssim D \lesssim 10 \text{ kpc}$) stars near $(l, b) = (60^\circ, -55^\circ)$, in the vicinity of the Aquarius constellation. Thus, the co-moving group was named the Aquarius stream. The stream is most apparent when examining heliocentric velocities against galactic latitude for stars within $-70^\circ < b < -50^\circ$. Williams et al. (2011) employed a selection criteria of $-250 \text{ km s}^{-1} < V_{\text{hel}} < -150 \text{ km s}^{-1}$, $30^\circ < l < 75^\circ$ and $J > 10.3$ to maximize the contrast between the stream and stellar background, identifying 15 stars in the process. The average heliocentric velocity of these members was found to be $V_{\text{hel}} = -199 \text{ km s}^{-1}$, with a dispersion of 27 km s^{-1} . The radial velocity uncertainties provided by the RAVE catalog are described to be $\sim 2 \text{ km s}^{-1}$, so the stream's wide velocity distribution appears to be real.

Through a statistical comparison with predictions of stellar positions and kinematics from the Galaxia (Sharma et al. 2011) and Besançon (Robin et al. 2003) models of the Milky Way, Williams et al. (2011) found the stream to be statistically significant ($> 4\sigma$). The choice of model, cell dimension, or extinction rate made no real difference to the detection significance. The authors concluded the over-density was genuine, and inferred that the co-moving group is a stellar stream. Based on the phase space information available, Williams et al. (2011) concluded that the newly discovered stream could not be positively associated with the Sagittarius or Monoceros stream, the Hercules-Aquila cloud, or either the Canis Major or Virgo over-densities.

RAVE data suggest the Aquarius stream has a metallicity of $[\text{Fe}/\text{H}] = -1.0 \pm 0.4 \text{ dex}$ ⁵, slightly more metal-rich than halo stars at the same distance ($[\text{Fe}/\text{H}] = -1.1 \pm 0.6 \text{ dex}$) after the same selection cuts had been employed. Of the 15 Aquarius stream stars in the Williams et al. (2011) discovery sample, the metallicity range determined from medium-resolution spectroscopy is wide: from $[\text{Fe}/\text{H}] = -2.02$ to -0.33 . High-resolution spectra with high S/N are necessary to accurately characterise the stream's metallicity distribution function (MDF).

To this end, Wylie-de Boer et al. (2012) obtained high-resolution ($\mathcal{R} = 25,000$) spectra with modest S/N ($\sim 30 \text{ pixel}^{-1}$) for six Aquarius stream stars using the echelle spectrograph on the Australian National University's 2.3m telescope. Their data indicate a surprisingly narrow spread in metallicity compared to previous work: $[\text{Fe}/\text{H}] = -1.09 \pm 0.10 \text{ dex}$, with a range extending only from -1.25 to -0.98 dex . Samples with such small dispersions in metallicity are typically observed in mono-metallic environments (e.g. globular or open clusters). The largest $[\text{Fe}/\text{H}]$ discrepancy between the Williams et al. (2011) and Wylie-de Boer et al. (2012) study was $\Delta[\text{Fe}/\text{H}] = -0.66 \text{ dex}$ for the most metal-rich star in the Williams et al. (2011) sample. The most metal-poor star in the Williams et al. (2011) study was not observed by Wylie-de Boer et al. (2012).

In addition to ascertaining stellar parameters, Wylie-

de Boer et al. (2012) measured elemental abundances for the Aquarius stream stars – the only study to date to do so. The authors primarily focussed on Na, O, Mg, Al, and Ni. These elements have been extensively studied in globular cluster stars, where unique abundance patterns are observed. Specifically, an anti-correlation between sodium and oxygen content appears ubiquitous to stars in globular clusters (Carretta et al. 2009). Wylie-de Boer et al. (2012) identified two stream stars with slightly higher $[\text{Na}/\text{Fe}]$ abundance ratios than halo stars of the same metallicity. No strong oxygen depletion was evident in the data, and no overall Na-O anti-correlation was present. Wylie-de Boer et al. (2012) also found $[\text{Ni}/\text{Fe}]$ abundance ratios similar to thick disk/globular cluster stars, markedly higher than those reported for the Fornax dwarf spheroidal (dSph) galaxy, which has a comparable mean metallicity to the Aquarius stream.

Combined with the low level of $[\text{Fe}/\text{H}]$ scatter present in their sample, these chemical abundances led Wylie-de Boer et al. (2012) to conclude that the Aquarius stream is the result of a tidally disrupted globular cluster. However, Williams et al. (2011) previously excluded this scenario after modelling an Aquarius-like progenitor infalling onto the Milky Way. The predicted positions and velocities from their simulations did not match any known globular cluster. If both scenarios are accurate, then the undiscovered disrupting cluster might still remain. It should also be quite close, such that its continued absence would be puzzling.

We seek to investigate the nature of the Aquarius stream, specifically the globular cluster origin claimed by Wylie-de Boer et al. (2012). Details of the observations and data reduction are outlined in the following section. The bulk of our analysis is presented in Section 3 and a thorough chemical abundance analysis is chronicled separately in Section 4. Uncertainties are outlined in Section 5. A detailed discussion of our results is made in Section 6, and we conclude in Section 7 with a summary of our conclusions and critical interpretations.

2. OBSERVATIONS & DATA ANALYSIS

The most complete sample of Aquarius stream stars is presented in the discovery paper of Williams et al. (2011). We have taken high S/N spectra for 5 Aquarius stream candidates using the Magellan Inamori Kyocera Echelle (MIKE) spectrograph (Bernstein et al. 2003) on the Magellan Clay telescope. Although these observations were carried out independently of the Wylie-de Boer et al. (2012) study, by chance there are four stars common to both samples. The additional star in this sample, C2306265-085103, was observed by the RAVE survey but had a S/N ratio too low for stellar parameters to be accurately determined. All program stars were observed in July 2011 in $\sim 1''$ seeing at low airmass (Table 1), and six standard stars were observed in March 2011. All observations were taken using a $1.0''$ slit without spectral or spatial binning, providing a spectral resolution in excess of $\mathcal{R} = 28,000$ in the blue arm and $\mathcal{R} = 22,000$ in the red arm. The exposure time for our program stars was 650 seconds per star in order to ensure a S/N ratio in excess of 100 pixel^{-1} at 600 nm.

Calibration frames were taken at the start of each night, including 20 flat-field frames (10 quartz lamp, 10 diffuse flats) and 10 Th-Ar arc lamp exposures for wave-

⁵ Williams et al. (2011) formally quote $[\text{M}/\text{H}]$, but for the sake of a consistent discussion we assume $[\text{M}/\text{H}] \equiv [\text{Fe}/\text{H}]$ throughout this study.

Table 1
Observations

Designation	α (J2000)	δ (J2000)	UT Date	UT Time	Airmass	Seeing ($'$)	t_{exp} (secs)	S/N ^a (px $^{-1}$)	V_{hel} (km s $^{-1}$)
Standard Stars									
HD 41667	06:05:03.7	-32:59:36.8	2011-03-13	23:40	1.01	1.0	90	340	297.1
HD 44007	06:18:48.6	-14:50:44.2	2011-03-13	23:52	1.03	1.0	120	280	161.8
HD 76932	08:58:44.2	-16:07:54.2	2011-03-14	00:16	1.16	1.0	25	330	117.8
HD 136316	15:22:17.2	-53:14:13.9	2011-03-14	09:37	1.12	0.9	120	400	-38.8
HD 141531	15:49:16.9	+09:36:42.5	2011-03-14	09:52	1.31	0.9	120	350	2.8
HD 142948	16:00:01.6	-53:51:04.1	2011-03-14	09:45	1.11	1.0	90	320	29.9
Program Stars									
C222531-145437	22:25:31.7	-14:54:39.6	2011-07-30	06:52	1.03	0.8	650	135	-156.4
C230626-085103	23:06:26.6	-08:51:04.8	2011-07-30	08:15	1.10	1.0	650	100	-221.1
J221821-183424	22:18:21.2	-18:34:28.3	2011-07-30	05:58	1.03	0.9	650	115	-159.5
J223504-152834	22:35:04.5	-15:28:34.9	2011-07-30	07:34	1.05	1.0	650	130	-169.7
J223811-104126	22:38:11.6	-10:41:29.4	2011-07-30	08:57	1.22	1.2	650	115	-235.7

^a S/N measured at 600 nm for each target.

length calibration. The data were reduced using the CarPy pipeline⁶. For comparison purposes one of the standard stars, HD 41667, was also reduced using standard extraction and calibration methods in IRAF. The resultant spectra from both approaches were compared for residual fringing, S/N , and wavelength calibration. No noteworthy differences were present, and the CarPy pipeline was utilised for the remainder of the data reduction. Each reduced echelle order was carefully normalised using a cubic spline with defined knot spacing. Normalised orders were stitched together to provide a single one-dimensional spectrum from 333 to 916 nm.

The white dwarf HR 6141 was observed in March 2011 as a telluric standard. The S/N ratio for HR 6141 exceeds that of any of our standard or program stars. Although the atmospheric conditions at Las Campanas Observatory are certain to change throughout the night and between observing runs, we are primarily using this spectrum to identify stellar absorption lines that are potentially affected by telluric absorption.

3. ANALYSIS

3.1. Radial Velocities

The radial velocity for each star was determined in a two step process. An initial estimate of the radial velocity was ascertained by cross-correlation with a synthetic spectrum of a giant star with $T_{\text{eff}} = 4500$ K, $\log g = 1.5$, and $[\text{Fe}/\text{H}] = -1.0$ across the wavelength range 845 to 870 nm. The observed spectrum was shifted to the pseudo-rest frame using this initial velocity estimate. Equivalent widths (EWs) were measured for ~ 160 atomic transitions by integrating fitted Gaussian profiles (see Section 3.2). In each case a residual line velocity was calculated from the expected rest wavelength and the measured wavelength. The mean residual velocity offset correction is small in all cases (< 1 km s $^{-1}$), and this residual correction is applied to the initial velocity measurement from cross-correlation. The final heliocentric velocities are listed in Table 1, where the typical uncertainty is ± 0.1 km s $^{-1}$. These velocities

agree quite well with those compiled by Williams et al. (2011) as part of the RAVE survey: the mean offset is $\langle \Delta V \rangle = 2.5 \pm 2.7$ km s $^{-1}$, demonstrating the accuracy of the velocities published in the RAVE catalog.

3.2. Line Measurements

For the measurement of atomic absorption lines, we employed the line list of Yong et al. (2005) with additional transitions of Cr, Sc, Zn, and Sr from Roederer et al. (2010). The list has been augmented with molecular CH data from Plez et al. (2008). Isotopic and hyperfine splitting data was taken from ?. For molecular features (e.g. CH), or lines with hyperfine and/or isotopic splitting (Sc, V, Mn, Co, Cu, Ba, La, Eu), we determined the abundance using spectral synthesis with the relevant data included. For all other transitions, abundances were inferred from curve-of-growth with measured EWs.

The EWs for all absorption lines were measured automatically using software written during this study. The local continuum surrounding every atomic transition is determined, and a Gaussian profile is iteratively fit to the absorption feature of interest. Our algorithm accounts for crowded or blended regions by weighting pixels as a function of difference to the rest wavelength. These algorithms and software will be fully outlined in a future contribution (Casey et al 2013d, in preparation). For this study we have verified our approach by comparing EWs of 156 lines measured by hand and tabulated in Norris et al. (1996). We only included measurements in the Norris et al. (1996) study that were not marked with questionable line quality parameters. Excellent agreement is found between the two studies, which is illustrated in Figure 1. The mean difference is a negligible -0.64 ± 2.78 mÅ, and no systematic trend is present. The scatter can be attributed to the lack of significant digits in the Norris et al. (1996) study, as well as the S/N of the data. Other studies (e.g. Frebel et al. 2013) using the same algorithm described here find better agreement for spectra with higher S/N ratios: 0.20 ± 0.16 mÅ when we compare our results with manual measurements by Aoki et al. (2007), and a difference of 0.25 ± 0.28 mÅ is found between manual measurements by Cayrel et al.

⁶ <http://code.obs.carnegiescience.edu/mike>

Table 2
List of Atomic Transitions and Equivalent Width Measurements for Program and Standard Stars

Wavelength (Å)	Species	χ (eV)	$\log g f$	Equivalent Width					(cont..)
				C222531-145437 (mÅ)	C2306265-085103 (mÅ)	J221821-183424 (mÅ)	J223504-152834 (mÅ)	J223811-104126 (mÅ)	
6300.30	O I	0.00	-9.72	45.4	66.9	38.5	32.8	17.9	
6363.78	O I	0.02	-10.19	19.5	28.3	13.0	18.8	...	
5688.19	Na I	2.11	-0.42	49.0	131.5	38.4	
6154.23	Na I	2.10	-1.53	24.1	38.9	...	48.5	...	
6160.75	Na I	2.10	-1.23	37.7	58.5	...	65.7	...	
6318.72	Mg I	5.11	-1.97	...	47.9	14.7	62.8	8.9	
6319.24	Mg I	5.11	-2.22	30.8	...	5.5	
6965.41	Mg I	5.75	-1.51	59.2	...	

Table 2 is published in its entirety in the electronic edition. A portion is shown here for guidance regarding its form and content.

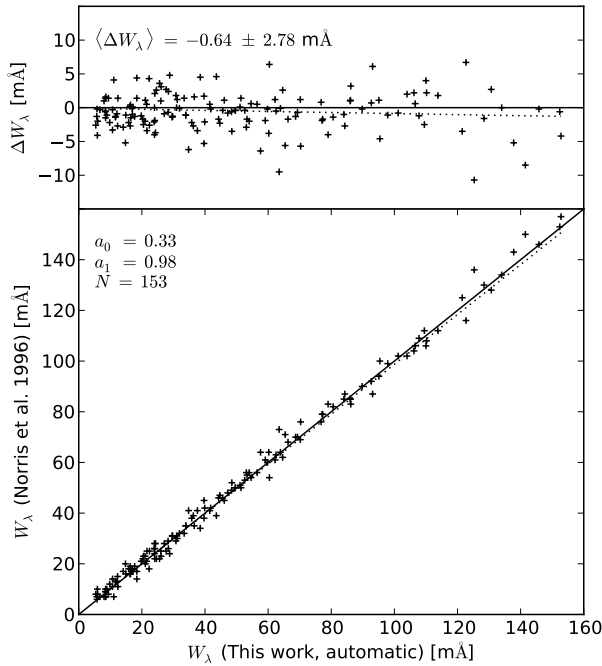


Figure 1. Comparison showing equivalent widths measured for HD 140283 using our automatic routine (see §3.2), and manual measurements by Norris et al. (1996). No systematic trend is present, and the mean difference between these studies is $\langle \Delta W_\lambda \rangle = -0.64 \pm 2.78 \text{ m}\AA$.

(2004) and our automatic results. Although we are extremely confident in our EW measurements, *every* absorption profile was repeatedly examined by eye for quality, and spurious measurements were removed.

We list the atomic data and measured EWs in Table 2. Transitions near the flat portion of the curve-of-growth have been excluded by removing measurements with reduced equivalent widths (REW), $\log_{10}(EW/\lambda) > -4.5$. A minimum detectable EW was calculated as a function of wavelength, S/N and spectral resolution by following Norris et al. (2001), and only lines that exceeded a 3σ detection significance were included for this analysis.

3.3. Model Atmospheres

We have employed the ATLAS9 plane-parallel stellar atmospheres of Castelli & Kurucz (2003). These

one-dimensional models ignore any centre-to-limb spatial variations, assume hydrostatic equilibrium and no convective overshoot from the photosphere. The stellar parameter spacing between models is 250 K in temperature, 0.5 dex in surface gravity, 0.5 dex in [M/H] and 0.1 dex in $[\alpha/\text{Fe}]$. We interpolated the temperature, gas and radiative pressure, electron density and opacities between atmosphere models using the Quickhull algorithm (Barber et al. 1996). Quickhull is reliant on Delaunay tessellation, which suffers from extremely skewed cells when the grid points vary in size by orders of magnitude – as T_{eff} values do compared to $\log g$ or $[(M,\alpha)/\text{H}]$. If unaccounted for, performing interpolation using such asymmetric cells can result in significant errors in atmospheric properties across all photospheric depths. We scaled each stellar parameter between zero and unity before interpolation to minimise these interpolation errors.

3.4. Stellar Parameters

The May 2011 version of the MOOG (Sneden 1973) spectral synthesis code has been used to derive individual line abundances and stellar parameters. This version employs Rayleigh scattering (Sobeck et al. 2011) instead of treating scattering as true absorption, which is particularly important for transitions blue-ward of 450 nm. This is noteworthy, but is less relevant for these analyses as most of the atomic transitions utilised here are red-ward of 450 nm.

3.4.1. Effective Temperature

The effective temperature, T_{eff} , for each star was found by demanding a zero-trend in excitation potential and line abundance for measurable Fe I transitions. The data were fitted with a linear slope, and gradients less than $|10^{-3}| \text{dex eV}^{-1}$ were considered to be converged. For comparison, photometric temperatures were calculated after our spectroscopic temperatures had been derived, and these are discussed in Section 3.4.4.

3.4.2. Microturbulence and Surface Gravity

The microturbulence for each star was found by forcing a zero-trend in the REW and abundance for Fe I lines. Similar to the effective temperature, linear slopes in REW and abundance of less than $|10^{-3}| \text{dex}$ were considered converged. The surface gravity for all stars was found by forcing the mean Fe I and Fe II abundances to be equal. The process is iterative: a zero trend with

Table 3
Stellar Parameters

Designation	This Study				Literature				Reference
	T_{eff} (K)	$\log g$ (dex)	v_t (km s $^{-1}$)	[Fe/H] (dex)	T_{eff} (K)	$\log g$ (dex)	v_t (km s $^{-1}$)	[Fe/H] (dex)	
Standard Stars									
HD 41667	4660	1.71	1.84	-1.20	4605	1.88	1.44	-1.16	Gratton et al. (2000)
HD 44007	4835	1.78	1.95	-1.77	4850	2.00	2.20	-1.71	Fulbright (2000)
HD 76932	5800	3.88	1.65	-1.05	5849	4.11	...	-0.88	Nissen et al. (2000)
HD 136316	4355	0.58	2.06	-1.93	4414	0.94	1.70	-1.90	Gratton & Sneden (1991)
HD 141531	4345	0.63	2.07	-1.69	4280	0.70	1.60	-1.68	Shetrone (1996)
HD 142948	5025	2.25	2.05	-0.74	4713	2.17	1.38	-0.77	Gratton et al. (2000)
Program Stars									
C222531-145437	4365	1.25	1.94	-1.22	4235 ± 118	1.45 ± 0.21	1.96 ± 0.11	-1.20 ± 0.14	Wylie-de Boer et al. (2012)
C230626-085103	4225	0.85	1.92	-1.13
J221821-183424	4630	0.88	2.16	-1.58	4395 ± 205	1.45 ± 0.35	1.96 ± 0.18	-1.15 ± 0.21	Wylie-de Boer et al. (2012)
J223504-152834	4650	2.16	1.55	-0.63	4597 ± 158	2.40 ± 0.14	1.47 ± 0.07	-0.98 ± 0.17	Wylie-de Boer et al. (2012)
J223811-104126	5190	2.93	1.62	-1.43	5646 ± 147	4.60 ± 0.15	1.09 ± 0.11	-1.20 ± 0.20	Wylie-de Boer et al. (2012)

the excitation potential, REW and abundances must be maintained.

3.4.3. Metallicity

The model atmosphere metallicity was exactly matched to that of our mean Fe I abundance. Individual Fe line abundances that were unusually deviant (e.g. $>3\sigma$) from the mean abundance were removed. The largest number of outlier measurements removed for any observation was nine for C222531-145437. These were transitions near the flat part of the curve-of-growth with REWs ~ -4.5 , leaving 60 Fe I and 10 Fe II lines for the analysis of C222531-145437. Usually only one outlier measurement was removed for the other candidates. The minimum number of Fe transitions employed for stellar parameter determination was 42 lines (33 Fe I and 9 Fe II), which occurred for our hottest star, J223811-104126.

3.4.4. Photometric Effective Temperatures

As a consistency check for our spectroscopic temperatures, we have estimated effective temperatures using the colour- T_{eff} empirical relationship for giant stars from Ramírez & Meléndez (2005). The $V - K$ colour has been employed as its calibration has the lowest residual fit. This relationship has a slight dependence on metallicity, and as such we have adopted the spectroscopic [Fe/H] values in Table 3 for these calculations. Optical V-band photometry has been sourced from the APASS catalogue (Henden et al. 2012), and K -band magnitudes have been sourced from the 2MASS catalog (Skrutskie et al. 2006). The reddening maps of Schlegel et al. (1998) estimate that the extinction for our stars varies between $E(B - V) = 0.03$ to 0.07 mags, and these values have been used to de-redden our $V - K$ colour.

Calculated photometric temperatures are listed in Table 4. The mean difference between the photometric temperatures and those found by excitation balance is -19 K, where the largest variation is -93 K for J223504-152834. While these photometric temperatures serve as a confirmation for our spectroscopically-derived values, for the remainder of this analysis we have employed effective temperatures determined by excitation balance.

Table 4
Reddening & Photometric Temperatures

Designation	$E(B - V)$ (mag)	$(V - K)_0$ (mag)	T_{phot} (K)	T_{spec} (K)	ΔT (K)
C222531-145437	0.03	2.86	4285	4365	-80
C230626-085103	0.05	3.00	4196	4225	-29
J221821-183424	0.03	2.36	4685	4630	+55
J223504-152834	0.04	2.50	4557	4650	-93
J223811-104126	0.07	1.84	5240	5190	+50

3.5. Distances

Many groups have determined distances for stars in the RAVE survey catalog, which includes all Aquarius stream members. Williams et al. (2011) tabulated a range of distances inferred by different techniques. Not every measurement technique was applicable to all Aquarius stars. The reduced proper motion distance technique was the only method to estimate distances for all Aquarius candidates. The variations between distance measurements are large. In particular, the distance for C222531-146537 ranged from 1.4 ± 0.1 kpc (Burnett & Binney 2010) to 10.3 ± 2.4 kpc (Breddels et al. 2010), where both groups claim to have the “most likely” distances.

Using the stellar parameters tabulated in Table 3, we have calculated distances by isochrone fitting. The Dotter et al. (2008) α -enhanced isochrones were used for these calculations, and an age of 10 Gyr was assumed for all stars (Williams et al. 2011; Wylie-de Boer et al. 2012). The closest point to the isochrone was found by taking the uncertainties in T_{eff} and $\log g$ (see Section 5) into account and measuring the distance modulus in the J band. Given the (i) number of uncertain measurements involved in calculating distances (T_{eff} , $\log g$, $E(B - V)$, J) and (ii) the resultant asymmetric uncertainties, distances were determined from 10,000 Monte-Carlo realisations. Table 5 lists the input parameters and uncertainties adopted for the Monte-Carlo realisations, as well as the emergent distances and uncertainties. Uncertainties in input parameters were assumed to be normally distributed. Of the distance scales collated in Williams et al. (2011), our distances are in most agreement with

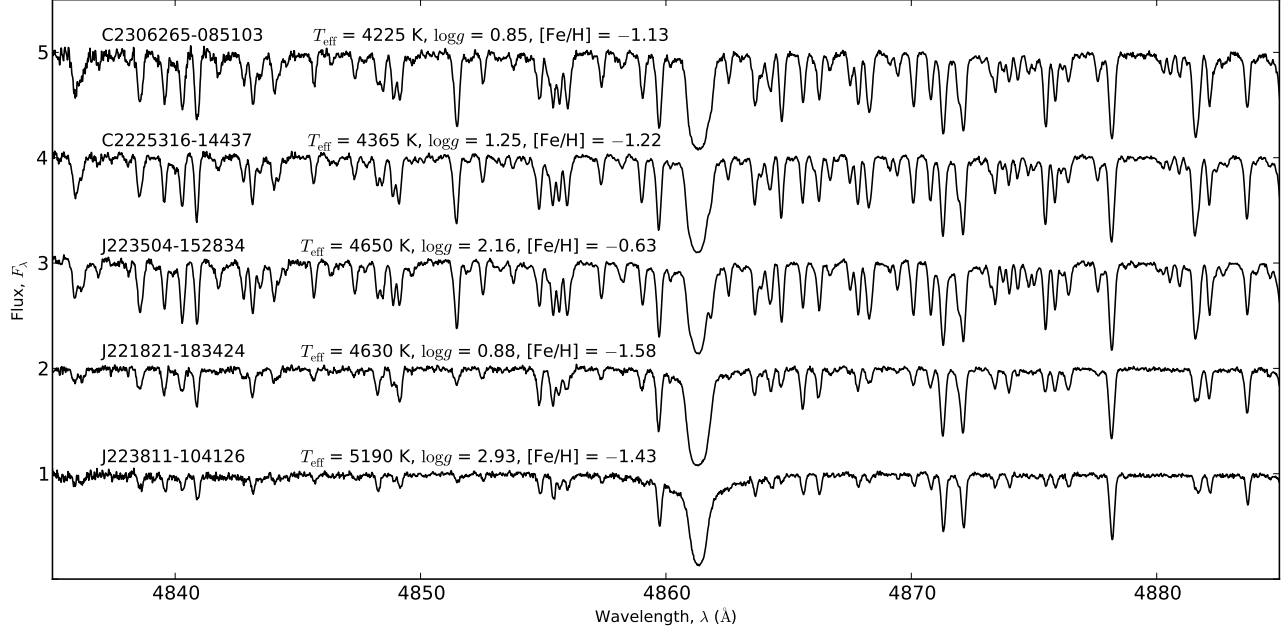


Figure 2. Normalised rest-frame spectra surrounding the H- β absorption line for all Aquarius stream candidates with offset fluxes. The effective temperature, surface gravity and metallicity is shown for all stars.

Table 5
Parameters and Uncertainties for Monte-Carlo Realisations

Designation	T_{eff} (K)	$\log g$ (dex)	J (mag)	$E(B-V)$ (mag)	V_{hel} (km s $^{-1}$)	μ_α (mas yr $^{-1}$)	μ_δ (mas yr $^{-1}$)	D (kpc)
C222531-145437	4365 ± 125	1.25 ± 0.20	10.341 ± 0.022	0.03 ± 0.01	-156.4 ± 0.1	3.5 ± 2.1	-14.7 ± 2.2	$5.1^{+1.1}_{-0.8}$
C230626-085103	4225 ± 125	0.85 ± 0.20	10.312 ± 0.025	0.05 ± 0.01	-221.1 ± 0.1	-2.5 ± 2.8	-15.4 ± 2.7	$6.5^{+1.4}_{-1.1}$
J221821-183424	4630 ± 125	0.88 ± 0.20	10.340 ± 0.021	0.03 ± 0.01	-159.5 ± 0.1	-10.6 ± 2.5	-19.3 ± 2.5	$5.6^{+1.3}_{-0.9}$
J223504-152834	4650 ± 125	2.16 ± 0.20	10.363 ± 0.025	0.04 ± 0.01	-169.7 ± 0.1	15.9 ± 2.2	-12.8 ± 2.2	$1.9^{+0.5}_{-0.4}$
J223811-104126	5190 ± 125	2.93 ± 0.20	10.420 ± 0.018	0.07 ± 0.01	-235.7 ± 0.1	-25.3 ± 2.1	-99.5 ± 2.1	$1.1^{+0.3}_{-0.2}$

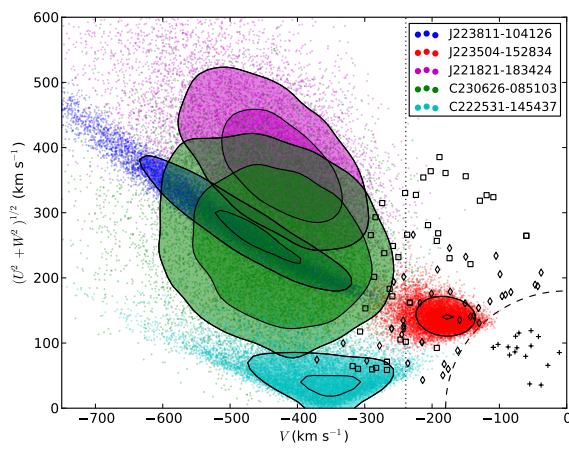


Figure 3. Galactic plane rotational velocities versus out-of-plane total velocities. The contours of each star represent the 68% and 95% confidence intervals from 10,000 Monte-Carlo realisations of the parameter distributions shown in Table 5. A sample of thick disc data from Nissen & Schuster (2010) is shown (+), as well as their high- and low-alpha halo populations (\diamond and \circ respectively).

the Zwitter et al. (2010) system. In fact, we find the

best agreement with the mean of all the distance scales tabulated in Williams et al. (2011). The uncertainties in our distance determinations are on the order of twenty per cent.

3.6. Dynamics

Velocity vectors and galactic orbits have been determined in the same Monte-Carlo realisations outlined in Section 3.5, which includes uncertainties in distances, proper motions⁷ and heliocentric velocities. We assume no uncertainty in on-sky position (α, δ). Orbital energy calculations have assumed a three-component (bulge, disc, halo) model of the Galactic potential that reasonably reproduces the Galactic rotation curve. The bulge is represented by a Hernquist potential:

$$\Phi_{\text{bulge}}(x, y, z) = \frac{GM_b}{r + a} \quad (1)$$

where $a = 0.6$ kpc. The disc is modelled as a Miyamoto-

⁷ The proper motions in Table 1 of Williams et al. (2011) are mis-associated to incorrect stars. This error was typographical; it did not affect the transverse velocity calculations (M.E.K. Williams, private communication). The proper motions listed in our Table 5 are correct.

Nagai potential (Miyamoto & Nagai 1975) where:

$$\Phi_{\text{disc}}(x, y, z) = \frac{GM_{\text{disc}}}{\sqrt{x^2 + y^2 + (b + \sqrt{z^2 + c^2})^2}} \quad (2)$$

with $b = 4.5$ kpc and $c = 0.25$ kpc and the Galactic halo is represented by a Navarro-Frenk-White dark matter halo (Navarro et al. 1997):

$$\Phi_{\text{halo}} = -\frac{GM_{\text{vir}}}{r [\log(1+c) - c/(1+c)]} \log\left(1 + \frac{r}{r_s}\right) \quad (3)$$

with the three components scaled such that the disc provides 85% of the radial force at R_{GC} , in order to yield a flat circular-speed curve at R_{GC} . The solar motion of Schönrich (2012) has been adopted, where $R_{\text{GC}} = 8.27$ kpc and a circular velocity speed $V_c = 238$ km s $^{-1}$.

The Aquarius stream members have bound orbits, all of which are probably retrograde except for J223504-152834 (Figure 3). Orbital energies and angular momenta from Monte-Carlo simulations are illustrated in Figure 4. The 16,686 stars from the Geneva-Copenhagen Survey sample (Nordström et al. 2004) are also shown as a reference, which primarily consists of nearby disc stars.

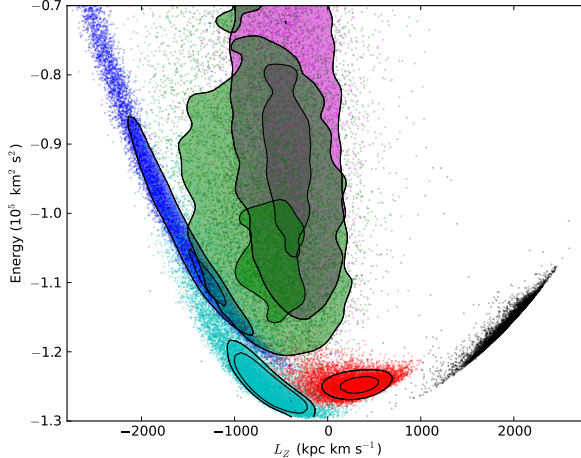


Figure 4. A Linblad ($L_Z - E$) diagram showing angular momenta and orbital energies after 10,000 Monte-Carlo realisations for each Aquarius stream star. Iso-contours represent the 68% and 95% confidence intervals. The black points without contours are from the Geneva-Copenhagen Survey sample (Nordström et al. 2004), which primarily consists of nearby disc stars and serves as a validation of our orbital energy calculations.

4. CHEMICAL ABUNDANCES

We have scaled our chemical abundances to Solar values using the chemical composition described in Asplund et al. (2009). The abundances for the standard and program stars are shown in Tables 6 and 7, respectively. The discussion of comparable elements are grouped accordingly.

4.1. Carbon

Carbon is produced by the triple- α process and ejected through supernovae events, or by mass-loss from asymptotic giant branch (AGB) stars (Kobayashi et al. 2011). The carbon abundance at the stellar surface increases as the star evolves along the AGB (e.g., Herwig 2005) owing to repeated third dredge-up events.

We have measured carbon abundances for all stars from the G-band head near 431.3 nm and the CH molecular feature at 432.3 nm, by comparing observed spectra with synthetic spectra for different carbon abundances. The synthetic spectra were convolved with a Gaussian kernel where the width was determined from nearby atomic lines with known abundances. Carbon was measured separately for both features, and in all stars the two measurements agree within 0.10 dex. An example fit to this spectral region for J223811-104126 is shown in Figure 5.

Carbon abundances in our standard stars agree well with the literature. For HD 136316 we find $[\text{C}/\text{Fe}] = -0.50 \pm 0.15$, where Gratton et al. (2000) find $[\text{C}/\text{Fe}] = -0.66$. Our $[\text{C}/\text{Fe}] = -0.48$ measurement for HD 141531 agrees with Gratton et al. (2000) to within 0.06 dex. Most program stars have near-solar carbon abundances, ranging from $[\text{C}/\text{Fe}] = -0.30$ for J221821-183424, and $+0.05$ for J223811-104126.

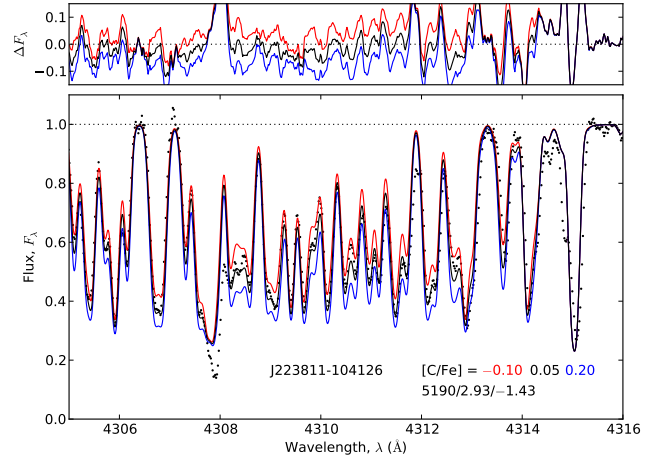


Figure 5. The carbon CH feature near 4313 Å in program star J223811-104126. The best-fit synthetic spectra is shown, with synthetic spectra for ± 0.15 dex about the best-fitting abundance.

4.2. Oxygen

Oxygen can be a particularly difficult element to measure. There are only a handful of lines available in an optical spectrum: the forbidden [O I] lines at 630 nm and 636 nm, and the O I triplet lines at 777 nm. The forbidden lines are very weak and become difficult to measure in hot and/or metal-poor stars ($[\text{Fe}/\text{H}] \lesssim -1.5$ dex). When they are present, depending on the radial velocity of the star, the [O I] lines can be significantly affected by telluric absorption. Moreover, the 630 nm line is blended with a Ni I absorption line (Allende Prieto et al. 2001). Hence the region requires careful consideration. Although the O I triplet lines at 777 nm are stronger than the forbidden lines, they are extremely susceptible to non-LTE effects, surface granulation (Asplund &

García Pérez 2001), and are sensitive to changes in microturbulence. Forbidden [O I] abundances in HD 136316 agree well with Gratton et al. (2000), where a difference of -0.07 dex is observed.

The [O I] lines were measurable in four of our Aquarius stream candidates. The 630 nm line in one of our candidates, C2306265-085103, was sufficiently affected by telluric absorption such that we deemed the line unrecoverable. Thus, only the 636 nm transition was used to derive an oxygen abundance for C2306265-085103. In our hottest star, J223811-104126, the forbidden oxygen lines were not detected above a 3σ significance. After synthesising the region, we deduce a very conservative upper limit of $[O/Fe] < 0.50$ dex from the [O I] lines. This is consistent with the rest of our candidates, with [O/Fe] abundances varying between 0.43 to 0.49 dex.

In order to derive an oxygen measurement for J223811-104126, we were forced to use the triplet lines at 777 nm. We extended these measurements for all Aquarius stars, and a mean abundance for each candidate was found from the synthesis of the permitted triplet lines. Oxygen abundances inferred from the triplet lines in all other stars were systematically $+0.27$ dex higher than abundances calculated from the [O I] forbidden lines. García Pérez et al. (2006) found the same result: [O/Fe] values based on the O I permitted triplet lines are on average $+0.19 \pm 0.07$ dex higher than those found from the forbidden lines, which did not include non-LTE corrections of $+0.08$ dex. Thus, we attribute our $+0.27$ dex offset between measurements of the [O I] and O I triplet lines to non-LTE and 3D effects. García Pérez et al. (2006) concluded that the forbidden lines, when not too weak, probably give the most reliable estimate of oxygen abundance. From the permitted O I triplet in J223811-104126, we derive an oxygen abundance of $[O/Fe] = 0.42 \pm 0.01$ dex (random scatter). This measurement will be systematically higher than the ‘true’ abundance if it were discernible from the [O I] lines, on the order of $\sim +0.27$ dex. When we apply this crude offset derived from the rest of our sample, we arrive at a corrected abundance of $[O/Fe] = 0.15 \pm 0.13$ dex (total uncertainty) for J223811-104126. This is the most oxygen-deficient star in our sample by a factor of two.

4.3. Sodium and Aluminium

Our line list includes three clean, unblended sodium lines at 568.8 nm, 615.4 nm and 616.1 nm. Not all three of these lines were detectable in each star. In the hottest and most metal-poor stars, J223811-104126 and J221821-183424 respectively, only the 568.8 nm line was measurable. For stars where multiple sodium lines were available, the line-to-line scatter is usually around 0.04 dex with a maximum of 0.09 dex in HD 41667. However, in calculating total abundance uncertainties (see Section ??) we have conservatively assumed a minimum random scatter of ± 0.10 dex for all stars.

Our [Na/Fe] abundances appear systematically higher than values found in the literature, on the order of 0.10 dex. For HD 142948 we find [Na/Fe] = 0.22, which is $+0.10$ dex higher than that found by Gratton et al. (2000), and similarly we find HD 76932 to be $+0.10$ dex higher than reported by Fulbright (2000). Gratton et al. (2000) also found HD 136316 to have [Na/Fe] = -0.29 dex, where we find [Na/Fe] = -0.14 , yet excellent

agreement is found in the stellar parameters in Gratton et al. (2000) and this study. Different solar compositions employed between this study and earlier work can account for ~ 0.08 dex of this effect, leaving the residual difference well within the observational uncertainties. However, it is important to note that the [Na/Fe] abundance ratios presented in this study may be slightly higher compared to previous studies.

There are six aluminium transitions in our optical spectra. The strongest of these lines occur at 394.4 nm and 396.1 nm and are visible in all of our stars. However this is a particularly crowded spectral region: the lines fall between the strong Ca H and K lines, with the 396.1 nm transition clearly located in the wing of the Ca H line. Additionally, the 394.4 and 396.1 nm lines have appreciable departures from the assumption of LTE, resulting in under-estimated abundances by up to ~ 0.6 dex (Bäumüller & Gehren 1997). Instead, we have measured Al abundances from other available transitions: the Al I lines at 669.6, 669.8, 783.5 and 783.6 nm. Generally the four Al I lines are in reasonable agreement with one another, yielding random scatter of less than 0.05 dex.

4.4. α -elements (*Mg, Si, Ca and Ti*)

The α -elements (Mg, Si, Ca and Ti) are forged through α -particle capture during hydrostatic burning of carbon, neon and silicon. Material enriched in α -elements is eventually dispersed into the interstellar medium following Type II core-collapse supernovae (SN).

Depending on the radial velocity of the star, some magnesium lines were affected by telluric absorption, particularly the 631.8 and 696.5 nm transitions. Atmospheric absorption was most notable for C222531-145437, where three of the four Mg transitions in our line list suffered some degree of telluric absorption, requiring an attentive correction. Every amended absorption profile was carefully examined, and lines with suspicious profiles were excluded from the final magnesium abundance. All $[\alpha/\text{Fe}]$ abundance ratios in the standard stars are in excellent agreement with the literature. Typically the difference is 0.01 dex, with the largest discrepancy of $\Delta[\text{Ti}/\text{Fe}] = +0.13$ dex for HD 76932 when compared with Fulbright (2000).

While Wylie-de Boer et al. (2012) find almost no scatter (± 0.02 dex) in [Mg/Fe] for stars common to both studies, we find C222531-145437 and J223504-152834 to be almost $+0.20$ dex higher than the rest of the sample. The reason for this [Mg/Fe] discrepancy is not obvious, given the stellar parameters between the two studies agree well, with the previously discussed exception in metallicity. Of the Mg I line profiles measured, only two transitions are common to both line lists: 631.8 nm and 631.9 nm. The oscillator strengths differ between studies; in these two lines the $\log gf$ differs by -0.24 and -0.27 dex respectively (our oscillator strengths are lower). This indicates that the difference in oscillator strengths may explain the ~ 0.2 dex offset in [Mg/Fe] between this study and Wylie-de Boer et al. (2012).

Of all the α -elements, calcium has the smallest measurement scatter in our stars. The mean was formed from four line measurements in each star, with a typical random scatter of 0.01 dex. Nevertheless, the aforementioned conservative minimum of 0.10 dex for random scatter applies, and uncertainties in stellar parameters

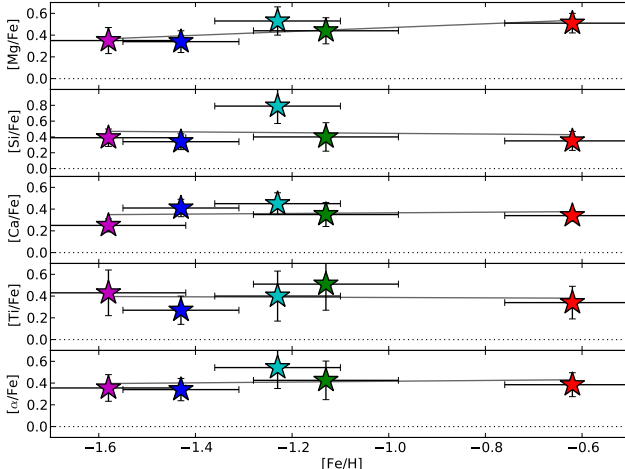


Figure 6. α -element abundances with respect to iron content. The mean $[\alpha/\text{Fe}]$ abundance from these is shown in the bottom panel. The Solar element-to-iron ratio is shown as a dotted line in each panel.

will contribute to the total error budget. As shown in Figure 6, all Aquarius stream candidates show super-solar $[\text{Ca}/\text{Fe}]$, ranging between $+0.23$ to $+0.43$ dex, consistent with $[(\text{Mg}, \text{Si}, \text{Ti})/\text{Fe}]$ measurements.

C222531-145437 has an unusually high silicon abundance ($[\text{Si}/\text{Fe}] = 0.79$), well outside the uncertainties of the rest of our sample. The 5 silicon line abundances in this star are in relatively good agreement with each other. If we exclude the highest measurement, then the mean abundance drops only slightly to $[\text{Si}/\text{Fe}] = 0.73 \pm 0.04$ (random scatter). The lowest silicon line abundance for C222531-145437 is $[\text{Si}/\text{Fe}] = 0.61$, which is still significantly higher than the mean abundance for any other star.

Titanium abundance ratios for the stream show typical levels of α -enhancement. Our mean titanium abundances are derived from four to seven clean, unblended lines. In our hottest and most metal-poor stars, no suitable Ti I transitions were available.

4.5. Iron-peak Elements

The Fe-peak elements (Sc to Zn) are primarily synthesized by the explosive nucleosynthesis of oxygen, neon, and silicon burning. Ignition can occur from Type II SN explosions of massive stars, or once a white dwarf

accretes enough material to exceed the Chandrasekhar mass limit and spontaneously ignite carbon, leading to a Type Ia SN.

Although not all Fe-peak elements are created equally, the Fe-peak elements generally exhibit similar trends with overall metallicity. All exhibit a positive trend with increasing iron abundance, with varying slope strengths.

The $[\text{Sc}/\text{Fe}]$ measurements presented in Figure 7 are averaged from six clean Sc II lines, and there is very little line-to-line scatter, the largest of which is 0.06 dex. The number of clean, suitable Cr I lines available between members fluctuated from three to twelve. Very little line-to-line scatter is present in both Cr I and Cr II : the random scatter is below 0.04 dex for most stars. Chromium abundances are only available for one of the standard stars, where our $[\text{Cr}/\text{Fe}] = 0.03$ is in excellent agreement with Fulbright (2000), where they find $[\text{Cr}/\text{Fe}] = 0.04$.

Manganese demonstrates a strong trend with increasing iron abundance (Figure 7). A significant source of Mn comes from Type Ia SN, and the strong Mn-Fe trend is consistent with chemodynamical simulations (Kobayashi & Nakasato 2011), as well as thick disc observations by Reddy et al. (2006). Although Mn is known to demonstrate significant departures from LTE, we have not applied any non-LTE corrections to our abundances.

Abundances of Co I lines were calculated by synthesis, as they demonstrate appreciable broadening due to hyperfine structure. Although they are known to suffer significant departures from LTE (Bergemann et al. 2010), no corrections have been made for these data. In general, $[\text{Co}/\text{H}]$ follows $[\text{Fe}/\text{H}]$ in our candidates. Cu abundances have also been determined by synthesis, and exhibit a strong positive relationship with increasing overall metallicity, consistent with MW trend???

Most Aquarius stream stars have seven clean Ni I transitions available. These lines are in excellent agreement, with a typical scatter of 0.03 dex. Nickel abundances have been published for two of our standard stars: HD 76932 (Fulbright 2000) and HD 141531 (Shetrone 1996). In both cases, our $[\text{Ni}/\text{Fe}]$ abundance ratios are slightly higher by $+0.08$ and $+0.10$ dex respectively. The different solar compositions employed by these studies can only account for 0.01 dex of this discrepancy, and the differences in oscillator strengths for common Ni I lines are negligible. Overall, the $[\text{Ni}/\text{Fe}]$ abundance ratios in the Aquarius stream stars do not deviate greatly

Table 6
Standard Star Abundances

Species	N	$\log \epsilon(X)$	σ_ϵ	[X/H]	[X/Fe]	Species	N	$\log \epsilon(X)$	σ_ϵ	[X/H]	[X/Fe]
HD 41667						HD 44007					
C (CH)	2	6.95	0.20	-1.48	-0.28	C (CH)	2	6.66	0.20	-1.77	-0.01
O I	2	7.95	0.06	-0.74	0.46	O I	1	7.41	0.00	-1.28	0.48
Na I	3	4.90	0.18	-1.34	-0.14	Na I	2	4.44	0.09	-1.80	-0.04
Mg I	4	6.72	0.10	-0.88	0.32	Mg I	2	6.30	0.06	-1.29	0.47
Al I	4	5.18	0.11	-1.27	-0.07	Al I	1	4.80	...	-1.65	0.11
Si I	5	6.55	0.06	-0.96	0.24	Si I	5	6.07	0.07	-1.44	0.32
K I	1	4.64	...	-0.39	0.81	K I	1	4.31	...	-0.72	1.04
Ca I	4	5.47	0.06	-0.87	0.33	Ca I	4	4.95	0.02	-1.39	0.37
Sc II	5	2.00	0.12	-1.15	0.05	Sc II	5	1.32	0.12	-1.85	-0.07
Ti I	4	3.96	0.04	-0.99	0.21	Ti I	1	3.48	...	-1.47	0.29
Ti II	3	4.09	0.25	-0.86	0.35	Ti II	4	3.47	0.15	-1.48	0.28
V I	4	2.85	0.11	-1.08	0.12	V I	1	2.22	...	-1.72	0.05
Cr I	10	4.22	0.08	-1.42	-0.22	Cr I	15	3.65	0.07	-1.99	-0.22

Continued..

Table 6
Standard Star Abundances

Species	<i>N</i>	$\log \epsilon(X)$	σ_ϵ	[X/H]	[X/Fe]	Species	<i>N</i>	$\log \epsilon(X)$	σ_ϵ	[X/H]	[X/Fe]
Cr II	2	4.54	0.05	-1.09	0.11	Cr II	3	4.00	0.01	-1.64	0.12
Mn I	3	3.87	0.04	-1.56	-0.36	Mn I	2	3.21	0.06	-2.22	-0.48
Fe I	61	6.30	0.12	-1.20	0.00	Fe I	51	5.74	0.13	-1.76	0.00
Fe II	13	6.35	0.05	-1.15	0.05	Fe II	15	5.74	0.10	-1.76	-0.00
Co I	3	3.73	0.06	-1.26	-0.06	Co I	0
Ni I	7	4.94	0.12	-1.28	-0.08	Ni I	4	4.47	0.05	-1.75	0.01
Cu I	1	2.29	...	-1.90	-0.70	Cu I	1	1.58	...	-2.61	-0.85
Zn I	2	3.36	0.08	-1.20	0.00	Zn I	2	2.83	0.05	-1.73	0.03
Sr I	1	1.31	...	-1.56	-0.36	Sr I	1	0.91	...	-1.96	-0.20
Y II	5	0.97	0.19	-1.24	-0.04	Y II	6	0.28	0.11	-1.93	-0.16
Zr I	2	1.42	0.05	-1.17	0.04	Zr I	0
Zr II	1	1.28	...	-1.30	-0.10	Zr II	1	0.59	...	-1.99	-0.23
Ba II	2	0.95	0.07	-1.23	-0.02	Ba II	2	0.31	0.06	-1.87	-0.11
La II	1	0.17	...	-0.93	0.27	La II	2	-0.57	0.05	-1.67	0.09
Ce II	4	0.35	0.18	-1.23	-0.02	Ce II	3	-0.41	0.12	-1.99	-0.23
Nd II	9	0.54	0.10	-0.88	0.32	Nd II	9	-0.36	0.11	-1.78	-0.01
Eu II	1	-0.13	...	-0.65	0.55	Eu II	1	-1.16	...	-1.68	0.08

HD 76932						HD 136316					
C (CH)	2	7.52	0.20	-0.91	0.14	C (CH)	2	5.95	0.20	-2.48	-0.50
O I	0	O I	1	7.17	...	-1.52	0.41
Na I	3	5.37	0.04	-0.87	0.18	Na I	2	4.17	0.04	-2.08	-0.14
Mg I	3	6.95	0.20	-0.65	0.40	Mg I	2	6.08	0.24	-1.52	0.41
Al I	4	5.45	0.07	-1.00	0.05	Al I	0
Si I	5	6.79	0.06	-0.72	0.33	Si I	4	5.89	0.05	-1.62	0.31
K I	1	4.94	...	-0.09	0.96	K I	1	3.91	...	-1.12	0.81
Ca I	4	5.60	0.02	-0.74	0.31	Ca I	4	4.71	0.02	-1.63	0.30
Sc II	4	2.10	0.05	-1.05	0.01	Sc II	4	1.20	0.08	-1.95	-0.02
Ti I	1	4.36	...	-0.59	0.46	Ti I	3	3.19	0.03	-1.76	0.17
Ti II	3	4.33	0.04	-0.62	0.44	Ti II	3	3.44	0.10	-1.51	0.42
V I	1	-3.33	...	-0.60	0.45	V I	3	1.85	0.01	-2.08	-0.15
Cr I	15	4.46	0.05	-1.18	-0.13	Cr I	12	3.49	0.05	-2.15	-0.22
Cr II	3	4.76	0.02	-0.88	0.17	Cr II	2	3.90	0.02	-1.74	0.19
Mn I	3	4.09	0.06	-1.34	-0.28	Mn I	3	3.09	0.03	-2.34	-0.41
Fe I	51	6.45	0.10	-1.05	0.00	Fe I	62	5.57	0.11	-1.93	0.00
Fe II	13	6.50	0.07	-1.00	0.05	Fe II	14	5.61	0.12	-1.89	0.04
Co I	1	3.94	...	-1.05	0.00	Co I	2	2.95	0.11	-1.09	-0.11
Ni I	5	5.29	0.02	-0.93	0.13	Ni I	5	4.22	0.11	-2.00	-0.07
Cu I	1	2.53	...	-1.66	-0.61	Cu I	1	1.36	...	-2.09	-0.16
Zn I	2	3.58	0.03	-0.98	0.07	Zn I	2	2.72	0.03	-1.83	0.10
Sr I	1	1.65	...	-1.22	-0.17	Sr I	1	0.53	...	-2.34	-0.41
Y II	5	1.14	0.05	-1.07	-0.02	Y II	7	0.12	0.11	-2.09	-0.16
Zr I	0	Zr I	1	0.79	...	-1.79	0.14
Zr II	0	Zr II	1	0.68	...	-1.90	0.03
Ba II	2	1.31	0.07	-0.87	0.18	Ba II	2	0.22	0.02	-1.96	-0.03
La II	1	0.50	...	-0.60	0.45	La II	1	-0.68	...	-1.78	0.16
Ce II	2	0.37	0.03	-1.21	-0.16	Ce II	5	-0.39	0.18	-1.97	-0.04
Nd II	3	0.56	0.06	-0.86	0.19	Nd II	10	-0.36	0.04	-1.78	0.15
Eu II	1	-0.33	...	-0.85	0.20	Eu II	1	-1.06	...	-1.58	0.33

HD 141531						HD 142948					
C (CH)	2	6.33	0.20	-2.10	-0.48	C (CH)	2	7.72	0.20	-0.71	0.03
O I	2	7.33	0.01	-1.35	0.34	O I	2	8.43	0.02	-0.26	0.47
Na I	2	4.28	0.05	-1.96	-0.27	Na I	3	5.73	0.13	-0.51	0.22
Mg I	2	6.30	0.15	-1.29	0.40	Mg I	3	7.24	0.12	-0.36	0.38
Al I	2	4.74	0.10	-1.71	-0.02	Al I	4	5.94	0.08	-0.51	0.23
Si I	5	6.03	0.10	-1.48	0.21	Si I	5	7.07	0.05	-0.44	0.30
K I	1	3.99	...	-1.04	0.65	K I	1	5.04	...	0.01	0.75
Ca I	4	4.90	0.03	-1.44	0.25	Ca I	4	5.78	0.01	-0.56	0.18
Sc II	5	1.40	0.11	-1.75	-0.06	Sc II	5	2.57	0.12	-0.58	0.16
Ti I	4	3.33	0.07	-1.62	0.07	Ti I	4	4.44	0.09	-0.51	0.23
Ti II	4	3.71	0.08	-1.24	0.46	Ti II	3	4.40	0.21	-0.55	0.19
V I	4	2.10	0.07	-1.83	-0.13	V I	5	3.31	0.04	-0.62	0.12
Cr I	12	3.68	0.06	-1.96	-0.27	Cr I	13	4.67	0.15	-0.97	-0.23
Cr II	2	4.11	0.02	-1.53	0.16	Cr II	3	4.88	0.03	-0.76	-0.02
Mn I	3	3.29	0.04	-2.14	-0.45	Mn I	3	4.45	0.06	-0.98	-0.24
Fe I	54	5.81	0.06	-1.69	0.00	Fe I	61	6.76	0.10	-0.74	0.00
Fe II	13	5.86	0.03	-1.64	0.05	Fe II	13	6.75	0.06	-0.75	-0.02
Co I	3	3.22	0.12	-1.77	-0.08	Co I	3	4.36	0.11	-0.63	-0.13
Ni I	7	4.42	0.12	-1.80	-0.11	Ni I	5	5.62	0.04	-0.60	0.13
Cu I	1	1.60	...	-2.59	-0.90	Cu I	1	3.10	...	-1.09	-0.35
Zn I	2	2.80	0.04	-1.76	-0.07	Zn I	2	3.89	0.06	-0.67	0.07
Sr I	1	0.66	...	-2.21	-0.52	Sr I	1	1.67	...	-1.20	-0.46

Continued..

Table 6
Standard Star Abundances

Species	<i>N</i>	$\log \epsilon(X)$	σ_ϵ	[X/H]	[X/Fe]	Species	<i>N</i>	$\log \epsilon(X)$	σ_ϵ	[X/H]	[X/Fe]
Y II	6	0.27	0.13	-1.94	-0.24	Y II	6	1.33	0.32	-0.88	-0.14
Zr I	0	Zr I	0
Zr II	1	0.75	...	-1.83	-0.14	Zr II	0
Ba II	2	0.39	0.05	-1.79	-0.10	Ba II	2	1.17	0.01	-1.01	-0.27
La II	1	-0.56	...	-1.67	0.03	La II	1	0.56	...	-0.54	0.20
Ce II	4	-0.31	0.12	-1.89	-0.20	Ce II	3	0.54	0.20	-1.04	-0.30
Nd II	10	-0.20	0.08	-1.62	0.07	Nd II	6	0.79	0.10	-0.63	0.11
Eu II	1	-0.95	...	-1.47	0.22	Eu II	1	0.08	...	-1.55	0.14

Table 7
Program Star Abundances

Species	<i>N</i>	$\log \epsilon(X)$	σ_ϵ	[X/H]	[X/Fe]	Species	<i>N</i>	$\log \epsilon(X)$	σ_ϵ	[X/H]	[X/Fe]
J221821-183424						C222531-145437					
C (CH)	2	6.55	0.20	-1.88	-0.30	C (CH)	2	7.15	0.20	-1.28	-0.05
O I	2	7.55	0.04	-1.13	0.45	O I	2	7.96	...	-0.73	0.49
Na I	1	4.75	...	-1.49	0.09	Na I	2	5.12	0.02	-1.12	0.10
Mg I	3	6.37	0.09	-1.23	0.35	Mg I	2	6.90	0.08	-0.70	0.53
Al I	1	5.08	...	-1.37	0.21	Al I	4	5.94	0.10	-0.51	0.71
Si I	5	6.32	0.08	-1.19	0.39	Si I	5	7.07	0.15	-0.44	0.79
K I	1	4.34	...	-0.69	0.89	K I	1	4.42	...	-0.61	0.62
Ca I	4	5.01	0.04	-1.33	0.25	Ca I	4	5.57	0.04	-0.77	0.45
Sc II	4	1.50	0.12	-1.65	-0.07	Sc II	4	2.08	0.13	-1.07	0.16
Ti I	0	Ti I	4	4.10	0.03	-0.85	0.37
Ti II	4	3.80	0.13	-1.15	0.43	Ti II	2	4.12	0.13	-0.83	0.40
V I	3	2.28	0.01	-1.65	-0.07	V I	5	2.91	0.10	-1.01	0.22
Cr I	11	3.80	0.06	-1.84	-0.26	Cr I	8	4.24	0.17	-1.40	-0.17
Cr II	2	4.07	0.03	-1.57	0.01	Cr II	1	4.38	...	-1.26	-0.03
Mn I	2	3.38	0.03	-2.05	-0.46	Mn I	3	3.98	0.05	-1.45	-0.23
Fe I	52	5.92	0.09	-1.58	0.00	Fe I	60	6.27	0.10	-1.23	0.00
Fe II	13	5.94	0.05	-1.56	0.02	Fe II	10	6.30	0.06	-1.20	0.03
Co I	1	3.32	...	-1.67	-0.09	Co I	4	3.77	0.09	-1.22	0.00
Ni I	5	4.61	0.14	-1.61	-0.03	Ni I	7	5.07	0.09	-1.15	0.08
Cu I	1	1.81	...	-2.38	-0.80	Cu I	1	2.72	...	-1.47	-0.24
Zn I	1	3.07	...	-1.49	0.09	Zn I	2	3.56	0.24	-1.00	0.23
Sr I	1	0.82	...	-2.05	-0.47	Sr I	1	1.55	...	-1.32	-0.09
Sr II	0	Sr II	0
Y II	3	0.44	0.02	-1.77	-0.19	Y II	5	1.78	0.16	-0.43	0.79
Zr I	0	Zr I	3	2.07	0.05	-0.51	0.72
Zr II	1	0.97	...	-1.61	-0.03	Zr II	0
Ba II	1	0.60	...	-1.58	0.00	Ba II	2	1.58	0.01	-0.60	0.62
La II	1	-0.58	...	-1.67	-0.09	La II	2	0.51	0.02	-0.59	0.64
Ce II	3	-0.39	0.06	-1.97	-0.39	Ce II	5	0.73	0.15	-0.85	0.37
Nd II	10	-0.22	0.07	-1.64	-0.06	Nd II	8	0.88	0.13	-0.54	0.69
Eu II	1	-0.86	-0.11	-1.38	0.20	Eu II	1	-0.29	...	-0.81	0.42

Species	<i>N</i>	$\log \epsilon(X)$	σ_ϵ	[X/H]	[X/Fe]	Species	<i>N</i>	$\log \epsilon(X)$	σ_ϵ	[X/H]	[X/Fe]
J223504-152834						J223811-104126					
C (CH)	2	7.71	0.30	-0.72	-0.10	C (CH)	2	7.05	0.25	-1.38	0.05
O I	2	8.50	0.10	-0.19	0.43	O I	1	8.27	...	-0.42	0.15 ⁸
Na I	3	5.87	0.12	-0.37	0.26	Na I	1	4.89	...	-1.35	0.08
Mg I	3	7.48	0.15	-0.12	0.51	Mg I	2	6.51	0.03	-1.09	0.34
Al I	3	6.12	0.09	-0.33	0.29	Al I	2	5.13	0.13	-1.32	0.11
Si I	5	7.24	0.10	-0.27	0.35	Si I	3	6.42	0.04	-1.09	0.34
K I	1	5.05	...	0.02	0.64	K I	1	4.50	...	-0.53	0.90
Ca I	4	6.06	0.03	-0.28	0.34	Ca I	4	5.32	0.03	-1.02	0.41
Sc II	5	2.65	0.10	-0.50	0.13	Sc II	2	1.60	0.03	-1.55	-0.12
Ti I	4	4.65	0.02	-0.30	0.32	Ti I	0
Ti II	1	4.67	...	-0.28	0.34	Ti II	4	3.79	0.09	-1.16	0.27
V I	4	3.50	0.11	-0.43	0.19	V I	1	2.45	...	-1.48	-0.05
Cr I	7	4.90	0.11	-0.74	-0.11	Cr I	12	4.10	0.06	-1.54	-0.11
Cr II	2	4.84	0.04	-0.79	-0.17	Cr II	3	4.34	0.07	-1.30	0.12
Mn I	3	4.66	0.04	-0.77	-0.15	Mn I	2	3.50	0.01	-1.93	-0.51
Fe I	63	6.88	0.12	-0.62	0.00	Fe I	33	6.07	0.06	-1.43	-0.00
Fe II	12	6.87	0.07	-0.63	-0.01	Fe II	9	6.04	0.07	-1.46	-0.03
Co I	3	4.39	0.09	-0.60	0.02	Co I	0
Ni I	7	5.64	0.09	-0.58	0.05	Ni I	2	4.84	0.04	-1.38	0.05
Cu I	1	3.72	...	-0.47	0.15	Cu I	1	1.96	...	-2.23	-0.80
Zn I	2	4.21	0.03	-0.35	0.27	Zn I	2	3.15	0.05	-1.41	0.02

Continued..

⁸ Abundance derived from the permitted O I triplet instead of the forbidden [O I] lines, see §4.2

Table 7
Program Star Abundances

Species	<i>N</i>	$\log \epsilon(X)$	σ_ϵ	[X/H]	[X/Fe]	Species	<i>N</i>	$\log \epsilon(X)$	σ_ϵ	[X/H]	[X/Fe]
Sr I	1	1.83	...	-1.04	-0.42	Sr I	1	1.23	...	-1.64	-0.21
Sr II	0	Sr II	0
Y II	3	1.80	0.03	-0.41	0.21	Y II	6	0.76	0.06	-1.45	-0.02
Zr I	3	2.26	0.05	-0.32	0.31	Zr I	0
Zr II	0	Zr II	0
Ba II	2	1.65	0.02	-0.53	0.10	Ba II	2	0.78	0.07	-1.40	0.03
La II	1	0.76	...	-0.34	0.28	La II	0
Ce II	3	0.87	0.13	-0.71	-0.09	Ce II	2	-0.07	0.02	-1.65	-0.22
Nd II	6	1.27	0.13	-0.15	0.47	Nd II	1	-0.25	...	-1.67	-0.24
Eu II	1	0.40	...	-0.12	0.50	Eu II	1	-0.55	...	-1.07	0.36

C2306265-085103					
C (CH)	2	7.20	0.20	-1.23	-0.10
O I	2	8.02	0.04	-0.67	0.46
Na I	2	5.31	0.01	-0.93	0.21
Mg I	2	6.90	0.06	-0.70	0.44
Al I	4	5.65	0.08	-0.80	0.33
Si I	5	6.78	0.08	-0.73	0.40
K I	1	4.46	...	-0.57	0.56
Ca I	4	5.56	0.04	-0.78	0.35
Sc II	3	2.15	0.09	-1.00	0.13
Ti I	4	4.13	0.03	-0.82	0.32
Ti II	3	4.32	0.35	-0.63	0.51
V I	4	2.85	0.06	-1.09	0.05
Cr I	3	4.13	0.12	-1.51	-0.38
Cr II	1	4.50	...	-1.14	-0.01
Mn I	3	4.10	0.05	-1.33	-0.20
Fe I	62	6.37	0.12	-1.13	0.00
Fe II	11	6.39	0.10	-1.11	0.02
Co I	3	3.88	0.06	-1.11	0.02
Ni I	7	5.11	0.07	-1.11	0.02
Cu I	1	2.96	...	-1.23	-0.10
Zn I	2	3.48	0.15	-1.08	0.05
Sr I	1	0.94	...	-1.93	-0.80
Sr II	0
Y II	4	1.26	0.26	-0.95	0.18
Zr I	3	1.60	0.05	-0.98	0.16
Zr II	0
Ba II	2	0.95	0.10	-1.23	-0.10
La II	1	0.07	...	-1.03	0.10
Ce II	2	0.09	0.02	-1.49	-0.36
Nd II	7	0.58	0.21	-0.84	0.29
Eu II	1	-0.41	...	-0.93	0.20

4.6. Neutron-capture Elements

Neutron-capture elements (Sr to Eu; $38 \leq Z \leq 63$) can be forged through multiple nucleosynthetic processes. The two primary processes that produce these elements are the rapid (*r*-) process and the slow (*s*-) process. While the *r*-process is theorised to occur in SN explosions, the *s*-process takes place foremost in AGB stars with a significant contribution from massive stars at higher metallicities (Meyer 1994, e.g.,), although models of rotating massive stars may change this picture (Frischknecht et al. 2012).

4.6.1. Strontium, Yttrium and Zirconium

These light neutron-capture elements generally increase in lock-step with each other. While [Y II/Fe] and [Zr I, Zr II/Fe] are in good agreement among all candidates, [Sr I/Fe] ratios are generally lower, with considerable scatter. The Sr II lines at 407.7 nm and 421.5 nm were not detected in any program or standard stars, although Sr I was measurable at 664.5 nm and no obvious telluric contamination was observed. Given that Sr I transitions are susceptible to non-LTE effects (Hansen et al. 2013), we note these Sr abundances should be

treated with some caution.

The Aquarius stream candidates have Y abundances consistent with halo field stars, with the exception of C222531-145437. With [Y/Fe] = 0.79, C222531-145437 is significantly over-abundant in Y for its metallicity (see Figure 4 of Travaglio et al. 2004). C222531-145437 is consistently over-abundant in Sr and Zr, too. All other program and standard stars have light *s*-process abundances and trends that are consistent with the chemical evolution of the Milky Way.

4.6.2. Barium and Lanthanum

Barium is primarily produced through the *s*-process, has appreciable hyperfine and isotopic splitting, and its measurement requires some careful consideration. Solar Ba isotopic ratios from ? have been adopted. Our standard stars have [Ba/Fe] abundances typical of the Milky Way halo. Two standard stars have existing [Ba/Fe] measurements from high-resolution spectra: HD 44007 and HD 76932. We find HD 44007 to have [Ba/Fe] = 0.03, which is in good agreement with Burris et al. (2000), who find 0.05 dex. For HD 76932 our measurement of [Ba/Fe] = 0.18 is in reasonable agreement with the Fulbright (2000) value of -0.02 dex, especially

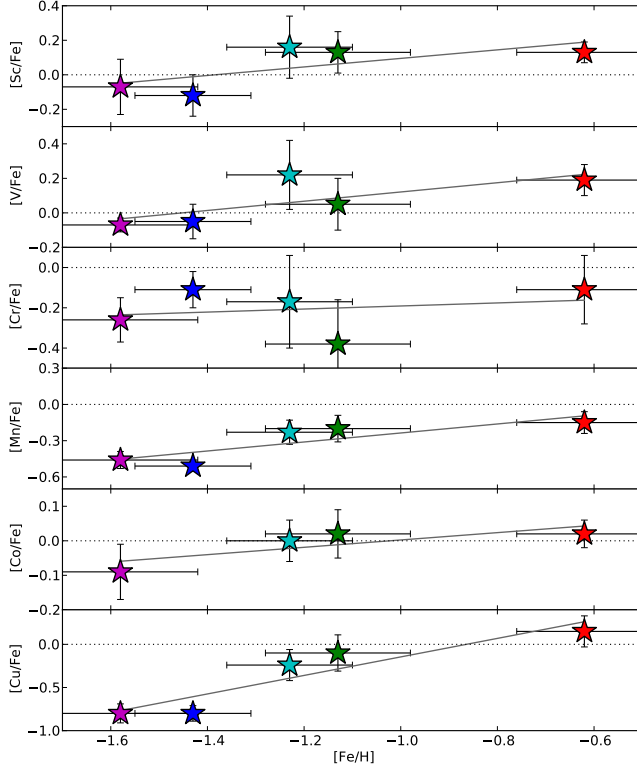


Figure 7. Iron peak element abundances (Sc, V, Cr, Mn, Co and Cu) with respect to iron for all Aquarius stream stars. Ni, an additional Fe-peak element, is discussed in §6.5 and shown in Figure 12

when differences in adopted solar composition are considered.

With one exception, the Aquarius stream candidates have $[\text{Ba}/\text{Fe}]$ abundance ratios that are indistinguishable from field stars, ranging between $[\text{Ba}/\text{Fe}] = -0.10$ to 0.10 dex. The exception is C222531-085103, which has an anomalously high barium abundance of $[\text{Ba}/\text{Fe}] = 0.62$. This is $\sim +0.60$ dex higher than the Milky Way trend at its given metallicity of $[\text{Fe}/\text{H}] = -1.26$. Our two Ba II lines in C222531-085103 are in excellent agreement with each other: $[\text{Ba}/\text{Fe}] = 0.63$, and 0.61 .

4.6.3. Cerium, Neodymium and Europium

Europium is primarily produced by the *r*-process, whereas the production of Ce and Nd is split between *s*- and *r*-process. Europium abundances have been determined by synthesising the 664.5 nm Eu II transition with hyperfine splitting data from ?.

We chose not to use the 643.7 nm line as it is appreciably blended by a nearby Si I line (Lawler et al. 2001), and our measurements were consistent with a hidden blend: the 643.7 nm Eu II abundance was systematically higher than the 664.5 nm counterpart. One Aquarius stream candidate, C222531-145437, appears enhanced in all $[\text{s-process}/\text{Fe}]$ abundance ratios compared to the program and standard sample. However no noteworthy difference in Eu, an *r*-process dominated element, was observed.

5. UNCERTAINTIES

5.1. Uncertainties in Stellar Parameters

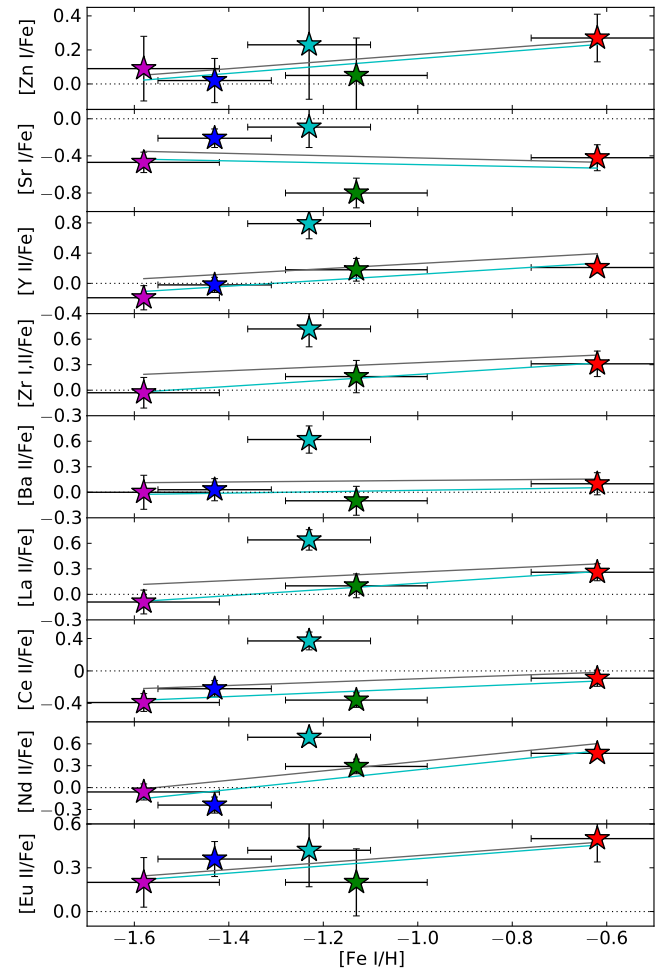


Figure 8. Element ratios for Aquarius stream stars. In the case of $[\text{Zr}/\text{Fe}]$, $[\text{Zr}_1/\text{Fe}]$ is taken where available and $[\text{Zr}_{\text{II}}/\text{Fe}]$ if no measurement was available for Zr I. See Table 7 for details.

Due to scatter in neutral iron lines measurements, there is a formal uncertainty in our calculated trend line between excitation potential and abundance, as well as between the reduced equivalent width and abundance. We have calculated $1-\sigma$ uncertainties in effective temperature and microturbulence by independently varying each stellar parameter until the relevant slope matches that formal uncertainty. This process is repeated for positive and negative offsets in temperature and microturbulence to allow for strong asymmetric uncertainty. The largest absolute offset is taken as the 1σ uncertainty. For surface gravity, the uncertainty has been calculated by varying $\log g$ until the difference in mean Fe I - Fe II abundance matches the standard error about the mean for Fe I and Fe II in quadrature. The calculated uncertainties are tabulated in Table 8.

These uncertainties ignore any correlations between stellar parameters, and therefore are likely to be underestimated. As such, we have assumed the total uncertainty in stellar parameters to be $\sigma(T_{\text{eff}}) = \pm 125$ K, $\sigma(\log g) = \pm 0.30$ dex, and $\sigma(v_t) = \pm 0.20$ km s $^{-1}$. These adopted uncertainties are higher than any of the measured the uncorrelated uncertainties, and are *extremely conservative*.

5.2. Uncertainties in Chemical Abundances

Table 8
Uncorrelated Uncertainties in Stellar Parameters

Designation	$\sigma(T_{\text{eff}})$ (K)	$\sigma(v_t)$ (km s $^{-1}$)	$\sigma(\log g)$ (dex)
HD 41667	53	0.09	0.13
HD 44007	81	0.29	0.09
HD 76932	107	0.08	0.19
HD 136316	33	0.15	0.12
HD 141531	25	0.05	0.13
HD 142948	47	0.10	0.11
J221821-183424	42	0.11	0.09
C222531-145437	46	0.05	0.12
J223504-152834	61	0.08	0.05
J223811-104126	49	0.16	0.08
C230626-085103	52	0.05	0.04

The uncertainties in chemical abundances are primarily driven by systematic uncertainties in stellar parameters, with a small contribution of random measurement scatter from individual lines. In order to calculate the abundance uncertainties due to stellar parameters, we have independently varied the stellar parameters by the adopted uncertainties, and measured the resultant change in chemical abundances. For lines requiring synthesis due to hyperfine structure, the difference in chemical abundances has been calculated from EWs. However, the effect of wing broadening due to hyperfine or isotopic splitting was generally small, and we can assume these effects are linear.

The abundance offsets from each variation of stellar parameters has been added in quadrature, along with the standard error about the mean for the line measurements. In some cases, the standard error about the mean is unrealistically small. As discussed earlier in Section 4.3, we have conservatively adopted an abundance floor of 0.10 dex for the standard deviation (i.e. $\text{Max}(0.10, \sigma(\log_e X))$). These resultant changes in abundances and total uncertainties are listed for all stars in Table 9. These total uncertainties have been used in all figures. This provides us with an uncertainty for all abundances, in all stars, of [X/H]. Generally though, we are most interested in the uncertainty in [X/Fe]. In order to calculate this uncertainty, the correlations in uncertainties due to stellar parameters between (X, Fe) need to be considered. We have followed the description in ? to calculate these correlations, and the overall uncertainties in [X/Fe], which are listed in Table 9 for all program and standard stars.

6. DISCUSSION

6.1. Stellar Parameter Discrepancies with Wylie-de Boer et al. (2012)

We seek to investigate the nature of the Aquarius stream. Specifically, the globular cluster origin suggested by Wylie-de Boer et al. (2012). For the four stars common to both samples, the stellar parameters reported in Wylie-de Boer et al. (2012) differ to our values listed in Table 3. Wylie-de Boer et al. (2012) deduce their stellar parameters by minimizing the χ^2 difference between the observed spectra and synthetic spectra from the Munari et al. (2005) spectral library. In general, effective temperatures between the two studies agree within the uncertainties. The only aberration is J223811-104126, where we find an effective temperature of 5190 K, \sim 450 K cooler

than the 5646 K found by Wylie-de Boer et al. (2012). Similarly, Williams et al. (2011) report a hotter effective temperature of 5502 K from low-resolution spectra. This is the largest discrepancy we see in any of our standard or program stars.

Photometric temperature relationships support our spectroscopic temperature for J223811-104126. The Ramírez & Meléndez (2005) relationship for giants suggests an effective temperature of 5240 K, which is 50 K warmer than our spectroscopically-derived temperature. Furthermore, the metallicity-independent $J - K$ colour- T_{eff} relationship for giants by Alonso et al. (1999) yields an effective temperature of 5215 K, 25 K warmer than our spectroscopic temperature. As a test, we set the temperature for J223811-104126 to be 5600 K – within the temperature regime reported by Williams et al. (2011) and Wylie-de Boer et al. (2012). The slopes and offsets in abundance with excitation potential and REW were large: $m_{\text{Fe I}} = -0.099 \text{ dex eV}^{-1}$, 0.162 dex, $m_{\text{Fe II}} = -0.133 \text{ dex eV}^{-1}$, -0.033 dex respectively, and in doing so we could not find a representative solution for this temperature.

Williams et al. (2011) and Wylie-de Boer et al. (2012) find J223811-104126 to be a sub-giant/dwarf, with a surface gravity $\log g = 4.16$ and 4.60 respectively. We note that the Williams et al. (2011) and Wylie-de Boer et al. (2012) effective temperatures for J223811-104126 are 150-300 K hotter than the Casagrande et al. (2010) $J - K$ photometric temperature calibration for dwarfs and sub-giants. We find the surface gravity for J223811-104126 to be $\log g = 2.93 \pm 0.30 \text{ dex}$, placing this star at the base of the red giant branch.

With the exception of J223811-104126, our surface gravities are largely in agreement with Wylie-de Boer et al. (2012). The only other noteworthy difference is for J221821-183424, where we find a lower gravity of $\log g = 0.88 \pm 0.30$ and Wylie-de Boer et al. (2012) find $\log g = 1.45 \pm 0.35 \text{ dex}$. Given the difference in the S/N between these studies, this difference is not too concerning. Wylie-de Boer et al. (2012) calculate the microturbulence from empirical relationships derived by Reddy et al. (2003) for dwarfs and Fulbright (2000) for giants. These relationships are based on the effective temperature and surface gravity. Our published microturbulent velocities agree excellently with the values presented in Wylie-de Boer et al. (2012), again with the exception of J223811-104126, where the difference in v_t is directly attributable to the offsets in other observables.

Of all the stellar parameters, metallicities exhibit the largest discrepancy between the two studies. In the Wylie-de Boer et al. (2012) study, after the stellar parameters (T_{eff} , $\log g$, v_t , and an initial [M/H] estimate) were determined through a χ^2 minimisation, the authors synthesised individual Fe I and Fe II lines using MOOG. Castelli & Kurucz (2003) stellar atmosphere models were employed (K. Freeman, private communication, 2013) – the same ones used in this study – albeit the interpolation schemes will have subtle differences. The median abundance of synthesised Fe I lines was adopted as the overall stellar metallicity, and scaled relative to the Sun using the Grevesse & Sauval (1998) Solar composition.

The study of Wylie-de Boer et al. (2012) is of slightly lower resolution ($\mathcal{R} = 25,000$ compared to $\mathcal{R} = 28,000$

Table 9
Abundance Uncertainties Due to Stellar Parameters

Species	$T_{\text{eff}} + 125 \text{ K}$	$\log g + 0.20 \text{ dex}$	$v_t + 0.30 \text{ km s}^{-1}$	$\text{Max}(0.10, \sigma) / \sqrt{N}$	Total Uncertainty	
	$\Delta_{\text{abundance}}$	$\Delta_{\text{abundance}}$	$\Delta_{\text{abundance}}$	(dex)	[X/H] (dex)	[X/Fe] (dex)
HD 41667						
O I	+0.03	+0.08	-0.01	0.07	0.11	0.12
Na I	+0.13	+0.00	-0.02	0.10	0.16	0.09
Mg I	+0.08	+0.01	-0.01	0.05	0.10	0.10
Al I	+0.10	+0.01	-0.01	0.06	0.11	0.07
Si I	+0.02	+0.03	-0.02	0.04	0.06	0.13
K I	+0.14	-0.03	-0.17	0.10	0.24	0.15
Ca I	+0.13	-0.01	-0.10	0.05	0.17	0.05
Sc II	-0.03	+0.08	-0.08	0.05	0.13	0.17
Ti I	+0.22	+0.01	-0.01	0.05	0.22	0.04
Ti II	-0.04	+0.07	-0.15	0.14	0.23	0.25
V I	+0.25	+0.01	-0.03	0.05	0.26	0.09
Cr I	+0.23	+0.00	-0.20	0.03	0.31	0.14
Cr II	-0.07	+0.08	-0.06	0.07	0.14	0.22
Mn I	+0.17	+0.01	-0.07	0.06	0.19	0.05
Fe I	+0.16	+0.01	-0.07	0.02	0.17	...
Fe II	-0.10	+0.08	-0.04	0.03	0.14	...
Co I	+0.18	+0.03	-0.01	0.04	0.19	0.04
Ni I	+0.12	+0.03	-0.01	0.05	0.13	0.03
Cu I	+0.19	+0.03	-0.16	0.10	0.27	0.10
Zn I	-0.03	+0.06	-0.09	0.07	0.14	0.19
Sr I	+0.24	+0.01	-0.06	0.10	0.27	0.11
Y II	+0.00	+0.08	-0.09	0.09	0.15	0.15
Zr I	+0.27	+0.01	+0.00	0.07	0.28	0.13
Zr II	+0.00	+0.08	-0.01	0.10	0.13	0.17
Ba II	+0.01	+0.06	-0.21	0.07	0.23	0.19
La II	+0.01	+0.07	-0.02	0.07	0.10	0.14
Ce II	+0.04	+0.08	-0.04	0.09	0.13	0.11
Nd II	+0.02	+0.06	-0.07	0.03	0.10	0.11
Eu II	-0.05	+0.04	-0.06	0.10	0.13	0.22

Table 9 is published for all standard and program stars in the electronic edition. A portion is shown here for guidance regarding its form and content.

presented here), but with a much lower S/N ratio: $\sim 25 \text{ pixel}^{-1}$ compared to $>100 \text{ pixel}^{-1}$ achieved here. The line list employed in the Wylie-de Boer et al. (2012) utilised astrophysical oscillator derived from a reverse solar analysis on the Solar spectrum. However, there are very few transitions listed in their line list: a maximum of 14 Fe I lines and 3 Fe II lines were available. For contrast, our analysis is based on 63 Fe I and 13 Fe II clean, unblended lines.

Suspecting the differing line lists may contribute to the metallicity discrepancy, we re-analysed our data using the Wylie-de Boer et al. (2012) line list and stellar parameters. Indeed, in doing so we arrive at reasonably similar metallicities to Wylie-de Boer et al. (2012). Without using their published stellar parameters *a priori*, in a “blind” analysis employing just the Wylie-de Boer et al. (2012) line list, we find stellar parameters similar to Wylie-de Boer et al. (2012). However, given the small numbers of lines used, even subtle changes to the stellar parameters can produce large variations to both the individual and mean Fe abundances. Additionally, we note that one Fe I transition at 642 nm in the Wylie-de Boer et al. (2012) line list was either not detected at the 3σ level – even though the S/N at this point exceeds 115 pixel^{-1} in every observation – or it was blended with a stronger neighbouring transition.

Given the overall data quality and the lack of suitable Fe lines available for analysis, it appears the Aquarius stream stars conspired to present a tight metallicity

distribution of $\sigma(\text{[Fe/H]}) = 0.10 \text{ dex}$. When viewed in light of enhanced [Ni/Fe] and [Na/Fe] abundance ratios, Wylie-de Boer et al. (2012) interpreted this chemistry as a signature of a globular cluster origin for the Aquarius stream.

6.2. The Aquarius Stream Metallicity Distribution

This study of high-resolution spectra with high S/N reveals a much broader metallicity distribution for the stream. With just 5 stars we find the metallicity varies from $\text{[Fe/H]} = -0.63$ to -1.58 dex . Although this is a small sample, we find the mean abundance and standard deviation to be $\text{[Fe/H]} = -1.20 \pm 0.33$.

If the metallicity dispersion were smaller, as found by Wylie-de Boer et al. (2012), a globular cluster scenario may be plausible. Classical globular clusters typically exhibit very little dispersion in metallicity. An intrinsic [Fe/H] dispersion of 0.33 dex – ignoring error contribution – is substantially larger than that seen in any globular cluster, with the exception of the unusual system ω -Centauri. In that cluster the total abundance range is about $\Delta \text{[Fe/H]} \sim 1.4 \text{ dex}$: from -2 to -0.6 (e.g. Marino et al. 2011), and many sub-populations have been identified (e.g., Johnson & Pilachowski 2010).

Other clusters with established intrinsic [Fe/H] dispersions include M54 – a nuclear star cluster of the Sagittarius dSph – where $\sigma_{\text{int}}(\text{[Fe/H]}) = 0.19$ (Carretta et al. 2010), and M22, where the interquartile range in [Fe/H] is $\sim 0.24 \text{ dex}$ (Da Costa et al. 2009; Marino et al. 2009, 2011). There are a few clusters where the

intrinsic dispersion is ~ 0.10 , namely NGC 1851 (Carretta et al. 2011), NGC 5824 (Saviane et al. 2012), and NGC 3201 (Simmerer et al. 2013). These globular clusters are outliers, and even in these unusual systems, only one or two system could plausibly match the abundance spread observed in the Aquarius stream (e.g. see Figure 4 in Simmerer et al. 2013). In fact, the Aquarius stream metallicity distribution – on its own – is large enough to be reconcilable with dSph galaxies like Fornax or Sagittarius, however the $\log(\bar{L}) - [\text{Fe}/\text{H}]$ relationship would suggest an extremely luminous system on the order of $L_{\text{tot}} \sim 10^{7.5} L_{\odot}$ (Kirby et al. 2011). However, the Aquarius stream stars exhibit $[\text{Ba}/\text{Y}]$ (e.g. heavy/light s-process) abundance ratios between -0.24 and $+0.19$, significantly lower than the $[\text{Ba}/\text{Y}] \geq 0.5$ level generally observed in the present day dSphs (Venn et al. 2004).

6.3. The Na-O Relationship

Extensive studies of stars in globular clusters have revealed variations in light element abundances, most notably an anti-correlation in sodium and oxygen content (see Norris & Da Costa 1995; Carretta et al. 2009, and references therein). This chemical pattern has been identified in every well-studied globular cluster, although the magnitude and shape of the anti-correlation varies from cluster to cluster.

Sodium is primarily produced through carbon burning in massive stars by the dominant $^{12}\text{C}(^{12}\text{C}, p)^{23}\text{Na}$ reaction. The final Na abundance is dependent on the neutron excess of the star, which slowly increases during carbon burning due to weak interactions (Arnett & Truran 1969). Massive stars ($> 10M_{\odot}$) eventually deliver their synthesized sodium to the interstellar-medium through SN II explosions. Because the eventual SN II explosion is devoid of any significant β -decay processes, the neutron excess of the ejected material is representative of the pre-explosive abundance. The ejected material eventually condenses to form the next generation of stars, which will have a net increase in their neutron excess with respect to their predecessors. Since the sodium production rate is correlated with the neutron excess, an overall increase in the total sodium content *and* Na-production rate between stellar generations can be expected. The sodium content also becomes important for production of nickel during the SN II event (see Section 6.5) because ^{23}Na is the only stable isotope produced in significant quantities during the C- or O-burning stages.

Oxygen depletion is likely the result of complete CNO burning within the stellar interior. The nucleosynthetic pathways that produce the Na-O anti-correlation are well understood to be proton-capture nucleosynthesis at high temperatures (Prantzos et al. 2007). However, the temperatures required to produce these patterns are not expected within the interiors of globular cluster stars. While the exact mechanism for which these conditions occur remains under investigation, we can describe the abundance variation as an external oxygen depletion (or dilution) model with time. Through comparisons with existing globular clusters, we can make inferences on the star-formation history of a system by measuring sodium and oxygen abundances in a sample of its stars.

Such inferences must be made with careful consideration. In addition to the normal care afforded for measuring elemental abundances from high-resolution spectro-

scopic data, attention must be given to telluric absorption, contamination from Ni I, as well as non-LTE and 3D effects when determining oxygen abundances. Furthermore, when characterising the oxygen depletion rate – the strength of the Na-O anti-correlation in a globular cluster – it is vital to sample, where possible, stars belonging to all three components (primordial, intermediate and extreme, see Carretta et al. 2009). If only a primordial sample of stars is observed, their $[\text{Na}/\text{Fe}]$ and $[\text{O}/\text{Fe}]$ abundances will be, by definition, indistinguishable from field stars of a similar metallicity. In such a scenario any inferred anti-correlation could equally be explained by small abundance variations or observational uncertainties.

Wylie-de Boer et al. (2012) measured sodium and oxygen abundances for four of their six Aquarius stream members. These measurements exist for only three stars common to both samples, as the data quality for J223811-104126 in the Wylie-de Boer et al. (2012) was too low to permit oxygen measurements. We have measured sodium and oxygen abundances for all of our stars, which are plotted in Figures 9 and 10. These figures employ the corrected $[\text{O}/\text{Fe}]$ value for J223811-104126 rather than a conservative upper limit (see Section 4.2).

The Wylie-de Boer et al. (2012) measurements show two stars with solar levels of $[\text{Na}/\text{Fe}]$ – identical to field star abundances for their metallicity – and two stars with enhanced sodium content: J223504-152834 and J232619-080808. We also find J223504-152834 to be sodium-enhanced, whereas the second star in their study, J232619-080808, is not in our sample. We find the additional star not present in the Wylie-de Boer et al. (2012) sample, C2306265-085103, to be sodium-enhanced to almost the same level of J223504-152834 with $[\text{Na}/\text{Fe}] = 0.26$. The sodium-enhanced stars exhibit no depletion of oxygen; their chemistry does not demonstrate a Na-O anti-correlation.

If the Aquarius stream is the result of a disrupted globular cluster, a large part of the picture must still be missing. Almost all of the Aquarius stream stars studied to date (either in this sample or the Wylie-de Boer et al. (2012) study), would be unambiguously classified as belonging to a “primordial” component, with chemistry indistinguishable from field stars. Identifying more Aquarius stream members belonging to the intermediate component with strong oxygen depletion, or perhaps members of an extreme component, would be convincing evidence for a Na-O anti-correlation and a globular cluster origin. Three stream stars identified to date (including two from this sample) might tentatively be classified as members of an intermediate population, with only a slight enhancement in sodium and no oxygen-depletion. Recall our $[\text{Na}/\text{Fe}]$ abundance ratios appear systematically higher in our standard stars when compared to the literature. Thus, if the strength of any Na-O relationship is to be used to vet potential disrupted hosts for the Aquarius stream, many more stream members will need to be identified and observed spectroscopically with high-resolution and high S/N . In the absence of such data, no evidence exists for a Na-O anti-correlation in the Aquarius stream.

6.4. The Al-Mg Relationship

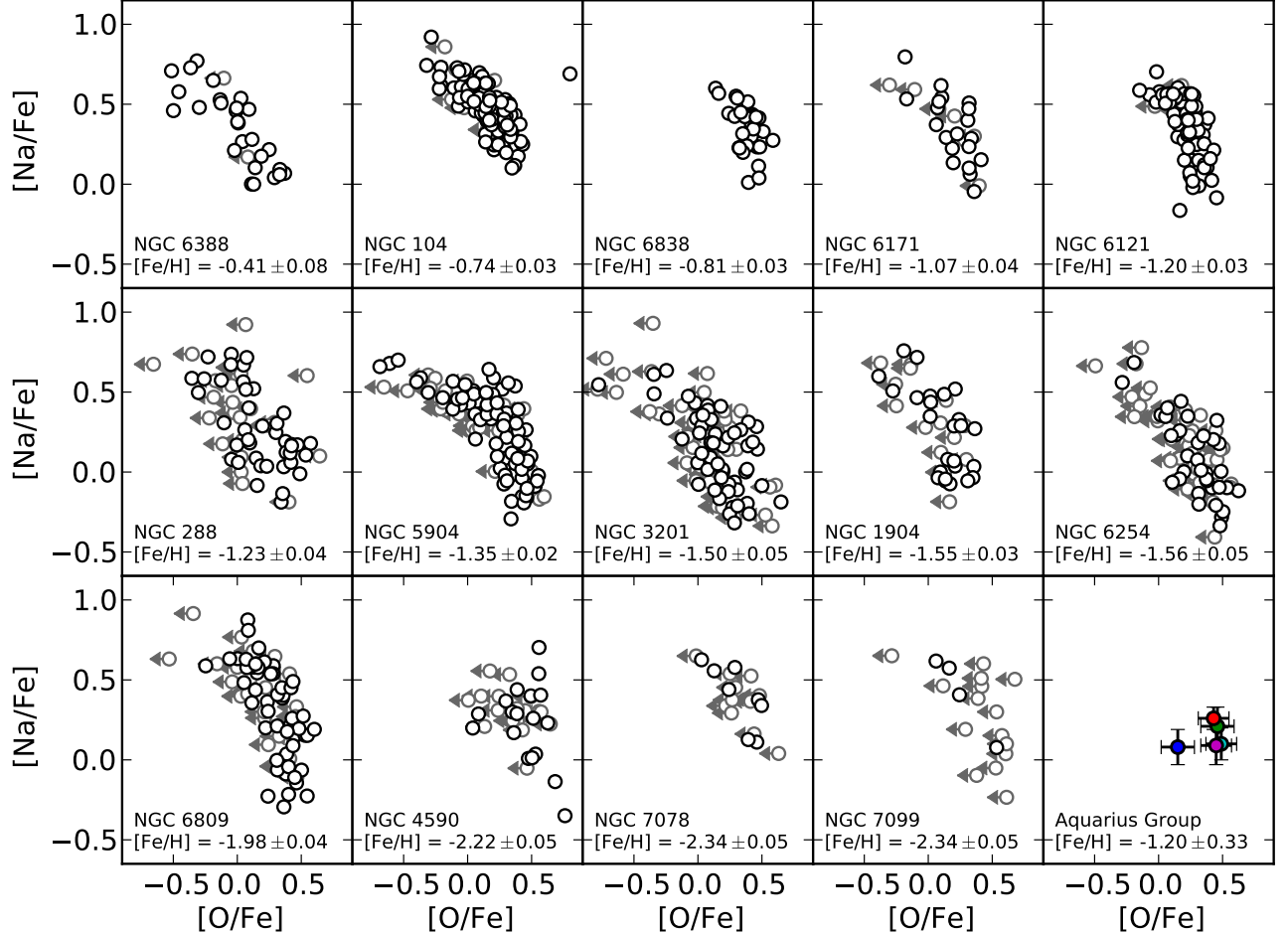


Figure 9. Oxygen and sodium abundances for 14 classical globular clusters from Carretta et al. (2009), demonstrating the clear inverse Na-O correlation, ubiquitous to all well-studied globular clusters. The $[O/Fe]$ and $[Na/Fe]$ abundances from this study for the 5 Aquarius stream stars (1/3 of the entire stream) are also shown in the last panel.

Although not ubiquitous to every system, many clusters exhibit an anti-correlation between aluminium and magnesium. This is perhaps unsurprising, given the nucleosynthetic pathways for these elements. In addition to the CNO cycle operating during hydrogen burning, the Mg-Al chain can also operate under extreme temperatures ($T \sim 8 \times 10^6$ K; Arnould et al. 1999). In these conditions, aluminium is produced by proton-capture of magnesium, beginning with ^{24}Mg to ^{25}Al . The relative lifetime of β -decay to proton-capture allows for the production of unstable ^{27}Si through proton-capture. Seconds later, the isotope decays to ^{27}Al , completing the ^{27}Si path of the Mg-Al chain. The alternative process onwards from ^{26}Al involves proton-capture to ^{26}Mg , but this process requires even higher temperatures ($T \sim 7 \times 10^6$ K).

The Mg-Al cycle can explain the observed anti-correlation observed in some globular clusters, and some AGB models can predict such a pattern (e.g., Ventura et al. 2011 but see nucleosynthesis yields from Karakas & Lattanzio (2007) and Karakas (2010)). Thus, while the pathways for creating these chemical patterns are understood, the temperatures required to produce this chain are much higher than expected for stellar interiors,

so the exact site and requisite conditions are lacking a full description.

Wylie-de Boer et al. (2012) published magnesium and aluminium abundances for five stars in their Aquarius sample. No inverse correlation is present in their data; their abundances are indistinguishable from field stars. The $[(\text{Mg, Al})/\text{Fe}]$ abundance ratios tabulated in Table 7 are generally in agreement with the Wylie-de Boer et al. (2012) sample, and we also find no Mg-Al anti-correlation. Given that we do not find a Na-O anti-correlation, it is not surprising that a Mg-Al anti-correlation is also not observed.

However it *is* surprising that we find such a strong positive relationship in $[\text{Mg}/\text{Fe}]$ and $[\text{Al}/\text{Fe}]$, with a best-fitting slope of $[\text{Al}/\text{Fe}] = 2.08 \times [\text{Mg}/\text{Fe}] - 0.57$. If we exclude the chemically peculiar star C222531-145437, the slope decreases to $[\text{Al}/\text{Fe}] = 0.96 \times [\text{Mg}/\text{Fe}] - 0.16$, a near 1:1 relationship. Even when a Mg-Al anti-correlation is not detected in globular clusters, there is generally more scatter in $[\text{Al}/\text{Fe}]$ at near-constant $[\text{Mg}/\text{Fe}]$ (e.g. see Figure 11 or Carretta et al. 2009). This is because Mg is much more abundant than Al, requiring only a small amount of Mg atoms to be synthesized to Al before the differences in $\log \epsilon_{\text{Al}}$ become appreciable, whilst the ob-

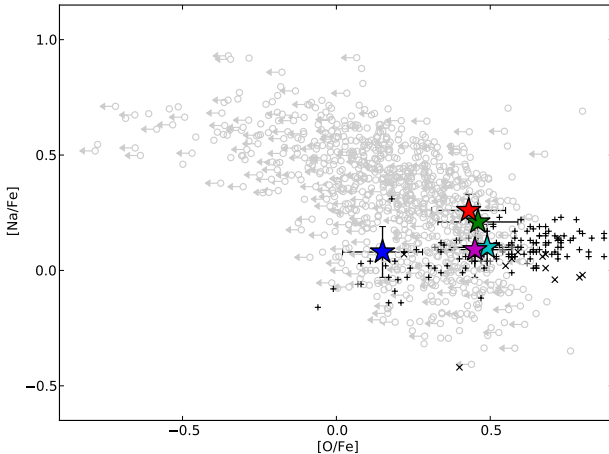


Figure 10. Oxygen and sodium abundances for thick disc (+), thin disc (x) and halo (o) stars from Reddy et al. (2006), and globular cluster stars from Carretta et al. (2009) (grey symbols). The Aquarius stream stars are also shown (●), illustrating how their [O/Fe], [Na/Fe] content is not dissimilar from Galactic stars. Ambiguous thick disc/thin disc stars in Reddy et al. (2006) are marked with thick disc symbols (+), as are uncertain thick disc/halo stars with halo symbols (o).

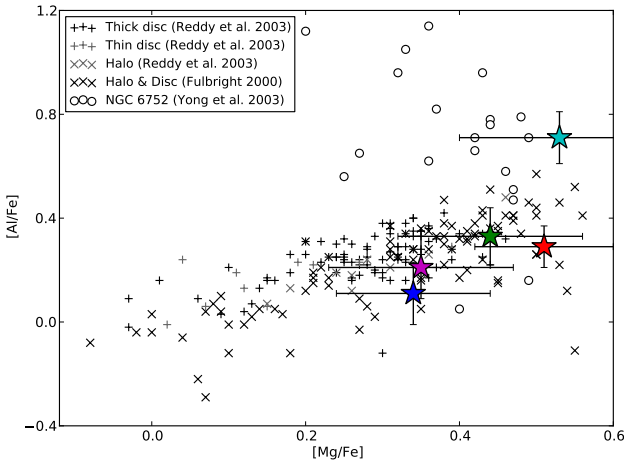


Figure 11. Magnesium and aluminium abundances for Aquarius stream stars (●), and Milky Way halo/disc stars from Reddy et al. (2003) (+) and Fulbright (2000) (○). The chemically peculiar star, C222531-145437, is marked.

served Mg abundance could remain within the uncertainties.

No classical globular clusters exhibit a positive correlation, and nor is such a pattern expected in globular clusters. However, a positive relationship between magnesium and aluminium can result from SN II contributions to the local interstellar medium. Intermediate-mass ($\gtrsim 4M_{\odot}$) AGB models can also contribute towards a positive correlation between aluminium and magnesium. Under extreme temperatures ($T \gtrsim 300 \times 10^6$ K), substantial ^{25}Mg and ^{26}Mg are produced by α -capture onto ^{22}Ne by the $^{22}\text{Ne}(\alpha, n)^{23}\text{Mg}$ and $^{22}\text{Ne}(\alpha, \gamma)^{26}\text{Mg}$ reactions respectively (e.g., Karakas et al. 2006). Depending on uncertain numerical details of the stellar model, the third dredge-up can mix significant quantities of ^{25}Mg and ^{26}Mg into the photosphere, even more than the quantity of ^{26}Al produced through the Mg-Al cycle. There-

fore, a positive relationship between magnesium and aluminium can occur if there has been significant contributions from intermediate-mass AGB stars (Karakas & Lattanzio 2003, but see results in Ventura et al. (2011)).

An unrealistically high fraction of intermediate-mass AGB stars would be required to produce the same chemical signature of a single SN II event. Given the efficiency of chemical mixing following supernovae, the observed positive Mg-Al correlation in the thick disc is likely the result of SN II events. Distinguishing between these processes observationally requires careful measurements of magnesium isotope abundances ^{24}Mg (indicating supernovae mixing), ^{25}Mg and ^{26}Mg (suggesting significant AGB contribution), which is not possible given our S/N or spectral resolution. In either scenario, we can summarise that the strong Mg-Al relationship provides additional chemical evidence against a globular cluster scenario for the Aquarius stream, and the chemistry is suggestive of Milky Way disc stars.

6.5. The Na-Ni Relationship

Detailed chemical studies of nearby disc stars have noted a correlation with [Na/Fe] and [Ni/Fe] abundance ratios. This relationship was first hinted in Nissen & Schuster (1997), where the authors found eight stars that were under-abundant in $[\alpha/\text{Fe}]$, [Na/Fe] and [Ni/Fe]. Interestingly, the authors noted that stars at larger galactocentric radii were most deficient in these elements. Fulbright (2000) saw a similar signature: stars with low [Na/Fe] were only found at large ($R_{\text{GC}} > 20$ kpc) distances. Nissen & Schuster (1997) proposed that since the outer halo is thought to have been largely built up by accretion, then the Na-Ni pattern may be a chemical indicator of merger history within the galaxy.

With additional data from Nissen & Schuster (2011), the Na-Ni relationship was found to be slightly steeper than originally proposed. The pattern exists only for stars with $-1.5 < [\text{Fe}/\text{H}] < -0.5$, and is not seen in metal-poor dSph stars (Venn et al. 2004), providing a potentially useful indicator for investigating chemical evolution. However, it is crucial to note that although there are only a few dSph stars in the $-1.5 < [\text{Fe}/\text{H}] < -0.5$ metallicity regime with [Na/Fe] and [Ni/Fe] measurements, they agree reasonably well with the Galactic trend.

The correlation between sodium and nickel content is the nucleosynthetic result of neutron-capture in massive stars. As previously discussed, the total Na abundance is controlled by the neutron excess, which limits the production of ^{58}Ni during SN II events. When the inevitable supernova begins, the core photodissociates into neutrons and protons, allowing the temporary creation of ^{56}Ni before it decays to ^{56}Fe . A limited amount of ^{54}Fe is also formed, which is the main source of production for the stable ^{58}Ni isotope through α -capture. When the core dissociates, the quantity of ^{54}Fe (and hence ^{58}Ni) produced is dependent on the abundance of neutron-rich elements during the explosion. As ^{23}Na is a relatively plentiful neutron source with respect to other potential sources (like ^{13}C), the post-supernova ^{58}Ni abundance is driven by the pre-explosion ^{23}Na content. Thus, through populations of massive stars undergoing C-burning, a positive correlation between sodium and nickel can be

expected.

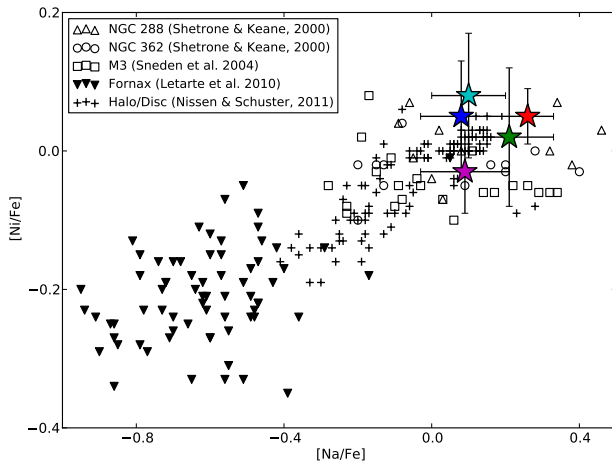


Figure 12. [Na/Fe] and [Ni/Fe] for Aquarius stream stars and for globular cluster, dSph, and field (halo/disc) stars. Stars from the most representative dSph galaxy, Fornax, are shown as downward triangles (\blacktriangledown). The Nissen & Schuster (2011) plotted sample included halo stars, as well as low- and high- α disc members. As noted by Nissen & Schuster (1997, 2011), a positive Na-Ni relationship exists for field stars, with dSph members exhibiting strong depletion in both elements and globular cluster stars consistently showing an enhancement. Sodium and nickel content for Aquarius members indicate a dSph accretion origin is unlikely.

Stars originating in dSph galaxies and globular clusters have very different chemical enrichment environments. Consequently, both types of systems exhibit chemistry that reflects their nucleosynthetic antiquity. Stars in dSphs do not demonstrate enhanced sodium or nickel content with respect to iron, as there has been a relatively small lineage of massive stars undergoing supernova. In contrast, globular cluster stars do have elevated [Na/Fe] and [Ni/Fe] signatures. This sharp contrast between dSph and globular cluster star chemistry is illustrated in Figure 12. Given the extended star formation within the Milky Way disc, globular cluster stars and disc stars are indiscernible in the Na/Ni plane: they both show an extended contribution of massive stars. The most that can be inferred from the Na and Ni abundances of Aquarius stream stars is that their enrichment environment is less like a dSph galaxy, and more representative of either a globular cluster, or the Milky Way disc.

6.6. The Chemically Peculiar Star C222531-145437

In almost every element with respect to iron, C222531-145437 is distinct from the other Aquarius stream stars. It is over-abundant in light refractory and neutron-capture elements, with a high barium abundance of $[\text{Ba}/\text{Fe}] = 0.68$. This value is well in excess of the halo ($[\text{Ba}/\text{Fe}] \sim 0.0$) – and our other Aquarius stream stars – which vary between -0.02 to 0.15 dex.

Here we discuss the possibility that an unseen companion has contributed to the surface abundances of C222531-145437. Although no radial velocity variations were observed between exposures, we do not have a sufficient baseline to detect such variation. The abundances of heavy elements produced by AGB stars have a high dependence on the initial metallicity and mass.

Low-mass ($\lesssim 3M_{\odot}$) AGB stars produce high fractions of heavy *s*-process elements compared to their light *s*-process counterparts. As such, [Ba/Y] is a useful indicator for considering contributions from a low-mass AGB companion. For C222531-145437, [Ba/Y] = -0.17, which is much lower than expected if a low-mass AGB star was responsible for the heavy element enhancements ([Ba/Y] ~ 0.5 as shown in Figure ??; see also Cristallo et al. (2009)). If mass transfer from an AGB companion has occurred very recently, non-negligible amounts of technetium are produced, remaining visible before it decays over ~ 100 Myr (Brown et al. 1990; Van Eck & Jorissen 1999; Uttenthaler et al. 2011). We saw no technetium absorption at the 404.9, 423.8 or 429.7 nm in the spectrum of C222531-145437. Intermediate-mass ($3-5M_{\odot}$) AGB stars also cannot explain the abundances for C222531-145437: using recently computed intermediate-mass AGB *s*-process yields for $3-5M_{\odot}$ for a star of [Fe/H] = -1.2 (C. Fishlock, in preparation) the resulting surface abundances do not match the observations. Therefore, we find no reason to suspect the heavy element enhancement in C222531-145437 is the result of mass transfer from an AGB companion.

Stars in ω -Centauri show large over-abundances of s -process elements compared to the Galaxy (Norris & Da Costa 1995; Stanford et al. 2010). M22 also hosts an s -process rich population (Marino et al. 2011). Like the Aquarius co-moving group, both clusters are relatively close to the Sun: 5.2 kpc and 3.2 kpc, respectively. M22 has a mean metallicity of $[\text{Fe}/\text{H}] \sim -1.7$ and a range between $-2.0 < [\text{Fe}/\text{H}] < -1.6$ dex, making an association between C222531-145437 and M22 unlikely. Similarly, C222531-145437 is unlikely to be associated with the metal-rich Argus association (IC 2391; De Silva et al. 2013), which also shows large enhancement in s -process abundances. Other groups have identified field stars enriched in s -process elements, which have generally been associated as tidal debris from ω -Centauri (Wylie-de Boer et al. 2010; Majewski et al. 2012). The high s -process abundance ratios and overall metallicity of C222531-145437 ($[\text{Fe}/\text{H}] = -1.22$) suggests this may be an additional tidal remnant.

ω -Centauri has a retrograde orbit with low inclination. Many groups simulating this orbit have predicted retrograde tidal debris to occur near the Solar circle (Dinescu 2002; Tsuchiya et al. 2003, 2004; Bekki & Freeman 2003). Subsequent searches for ω -Centauri debris in the Solar neighbourhood have led to tantalising signatures of debris. From over 4,000 stars targeted by Da Costa & Coleman (2008), only six candidate debris members were recovered, consistent with tidal stripping occurring long ago. Using data from the Grid Giant Star Survey (GGSS), an all-sky search looking for metal-poor giant stars, Majewski et al. (2012) identified 12 stream candidates. In addition, Majewski et al. (2012) performed 4,050 simulations in order to predict likely locations for ω -Centauri tidal debris. The results of their simulation are replicated in Figure 13, where the location of C222531-145437 is also shown. The velocity and position of C222531-145437 align almost precisely where Majewski et al. (2012) predict a high probability of tidal debris. More interestingly, the angular momentum and orbital energy for C222531-145437 (Figure ??) matches excellently for ω -Centauri cluster stars as well

as its previously identified tidal remnants (Wylie-de Boer et al. 2010). The chemical and phase-space information strongly suggests that C222531-145437 is associated with the remnant of tidal stripping that occurred as the proto- ω -Centauri fell into the Galaxy (Bekki & Freeman 2003).

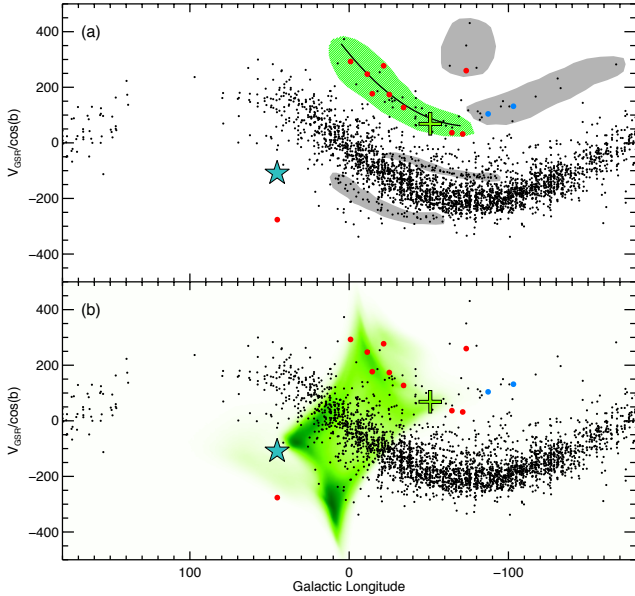


Figure 13. Panel (a) shows the distribution of giant stars in the GGSS (Majewski et al. 2012) in Galactic longitude and $V_{\text{GSR}}/\cos(b)$ after excluding stars with $|b| > 60^\circ$. Stars from the GGSS sample believed to be ω -Centauri tidal debris are shown in green shading. Red points are stars from the GGSS sample with abundances that follow the ω -Centauri $[\text{Ba}/\text{Fe}]$ – $[\text{Fe}/\text{H}]$ pattern. Blue points are those with high-resolution spectra that do not follow this trend. Grey shading highlights other potential halo substructures from their study. Panel (b) shows the probability distribution of ω -Centauri tidal debris from 4,050 simulations. The ω -Centauri core is shown as a green cross and the cyan star represents C222531-145437, falling almost precisely where a relatively high probability of ω -Centauri tidal debris is expected.

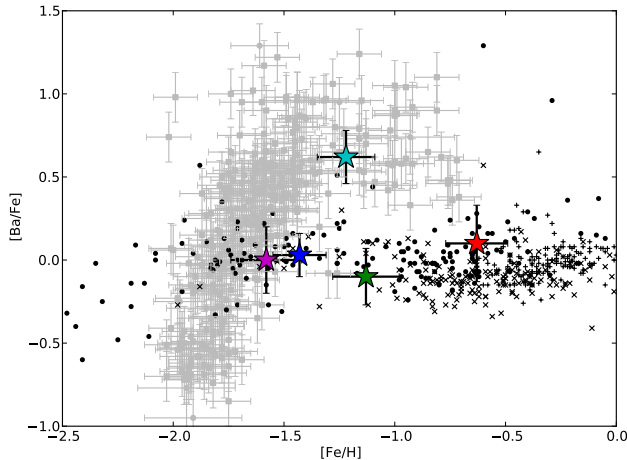


Figure 14. $[\text{Fe}/\text{H}]$ and $[\text{Ba}/\text{Fe}]$ for halo/disc stars (black) from Fulbright (2000); Reddy et al. (2003, 2006) and ω -Centauri RGB stars (grey) from Francois et al. (1988); Smith et al. (2000); Marino et al. (2011). Similar trends are observed for other heavy elements in ω -Centauri members. The candidate we associate with ω -Centauri tidal debris, C222531-145437, is marked in cyan.

In the Aquarius stream discovery paper, Williams et al. (2011) attempted to exclude possible known progenitors for the Aquarius stream. On the basis of metallicity, distance, proper motions, transverse velocities and orbital energies, the authors were able to exclude all known Milky Way satellites with the notable exception of ω -Centauri. Although the Aquarius stream metallicity distribution is not dissimilar from a known sub-population in ω -Centauri, the individual chemical abundances are quite distinct. The strong *s*-process enhancement with overall metallicity is not observed in the rest of our sample. Thus, with the exception of C222531-145437, the Aquarius members do not have a chemistry that is synonymous with ω -Centauri tidal debris. It will be most interesting to learn how many other members of the Aquarius stream are tidal remnants of ω -Centauri, given the frequency of these objects is quite low (e.g. see Da Costa & Coleman 2008; Majewski et al. 2012).

6.7. Disrupted Disc/Halo Stars – Signature of a Disc-Satellite Interaction?

Since the Aquarius stream is kinematically coherent, it has been assumed that the co-moving group has been accreted onto the Milky Way from a tidally disrupted satellite. The chemical abundances presented in this study do not favour an accretion scenario from a globular cluster or a dSph; there is conflicting evidence for either hypothesis. As it stands, the co-moving group appears chemically indistinguishable from thick disc/halo stars. These results force us to consider other scenarios that may replicate the observations.

The Aquarius stream has an unusually wide intrinsic velocity distribution. Generally a stellar stream is considered kinematically “cold” when its velocity dispersion is $\lesssim 8 \text{ km s}^{-1}$. We find the velocity dispersion from five members to be $\sim 30 \text{ km s}^{-1}$, consistent with Williams et al. (2011). Hypotheses invoked to explain the Aquarius co-moving group must account for the high velocity dispersion.

There are other co-moving groups in the Milky Way that were initially considered as tidal tails from disrupted satellites, that are now explainable as signatures of galaxy formation that are not specific accretion events. Like the Aquarius group, the Hercules moving group is significantly offset from the bulk of the observed velocity distribution. Members of the Hercules group exhibit a wide range of metallicities and ages (Bensby et al. 2007; Bovy & Hogg 2010). Furthermore, Hercules group stars have $[\text{X}/\text{Fe}]$ abundance ratios at a given $[\text{Fe}/\text{H}]$ that are *not* substantially different from the thin or thick disk. The Hercules group kinematics are well replicated in simulations by stars in the outer disk resonating with the bar in the central region of the Milky Way (Dehnen 2000; Fux 2001), and strong predictions are made for disk velocity distributions that would lend further weight to this hypothesis (Bovy 2010). The Canis Major stellar over-density was also first considered to be an accretion feature from the postulated Canis Majoris dSph galaxy (Martin et al. 2004). However, Momany et al. (2004) demonstrate that the star counts, proper-motions, photometry and kinematics of the “accreted feature” can be easily explained by the warp and flare in the outer thick disk. The Monoceros ring (Newberg et al. 2002; Jurić et al. 2008) is perhaps another example of such

an occurrence, as similar features naturally emerge as a consequence of galaxy-satellite interactions (Purcell et al. 2011), which has prompted considerable discussion (Lopez-Corredoira et al. 2012). It is clear that not all kinematic groups are attributable to accretion events; in many scenarios a galactic origin is more likely, and simpler.

We hypothesise that the Aquarius group is the result of displaced stars from a perturbation in the thick disc. That is, the stars are Galactic in origin but have been displaced by a disc-satellite interaction. Minor mergers can significantly disrupt the host galaxy (Villalobos & Helmi 2008), producing extended spatial and kinematic structure in the process. Minchev et al. (2009) proposed that such a perturbation would cause a galactic “ringing” effect in the neighbourhood surrounding the merger site, analogous to the resulting compression wave propagating outwards from a stone falling in water. Stars move closer together in the wave peak, a signature which is observable in the velocities and orbital motions of nearby stars. This signature is most prominent in the $U-V$ velocity plane as concentric circles (Gómez et al. 2012a), and dissolves over time (a few gigayear, depending on the mass of the perturber). After the $U-V$ velocity signature dissipates, a clear signature in angular momentum and orbital energy (L_Z, E) persists for long periods following the merger (e.g. see Gómez et al. 2012a).

Through Milky Way-Sagittarius simulations, Purcell et al. (2011) found that these disc-satellite interactions can explain ringing perturbations within the disc. Additionally, Widrow et al. (2012) and Gómez et al. (2012b) independently observed these phenomena – a “wavelike perturbation”, as Widrow described – in the SDSS and SEGUE catalogues. More recently, Gómez et al. (2013) proposed that these patterns were induced by the Sagittarius dSph interacting with the disc. Their simulations reproduce the observed north-south asymmetries and vertical wave-like structure, and show that the amplitude of these oscillations is strongly dependent on galactocentric distance. Combined with the oscillating vertical motions with the $U-V$ velocity pattern, corrugated waves are observed as a result of the interaction.

The stars in these oscillations should exhibit a wide range of ages, metallicities and a large spread in velocity dispersion. Thus, resultant oscillations following a disc-satellite interaction can satisfactorily explain the existence of the Aquarius co-moving group. We do not observe a distinct coherence in the $U-V$ velocity plane in our data, but the angular momentum and orbital energies for Aquarius members qualitatively reproduces the theoretically predicted pattern by Gómez et al. (2012a) in a retrograde direction. The extent and gradient of this L_Z-E signature is dependent on the mass of the perturber and the time since infall. Although our sample size is minute – and the sample size would still be small even if all Aquarius members had reliable orbits – the fact that we see no $U-V$ velocity coherence (Figure 3) is consistent with the observed L_Z-E pattern: signatures in the L_Z-E plane (Figure ??) become more extended over time as the $U-V$ signature dissipates. This is consistent with a disc-satellite interaction occurring in the disc approximately a few gigayear ago.

The Aquarius co-moving group resides at a intermediate latitude ($b \approx -55^\circ$) and with a radial distance of up

to ~ 5 kpc for some stars, the stars are slightly out of the plane. This is not inconsistent with a disc-satellite interaction. Gómez et al. (2013) find that a significant fraction of the total energy goes into vertical perturbations. While the mean vertical distance $\langle Z \rangle$ in their simulations are near zero, this is an average of disc particles at all plane heights – positive and negative – and the dispersions around $\langle Z \rangle$ are very large (F. Gómez, private communication, 2013). Moreover, Gómez et al. (2013) were only able to reliably track particles up to $|Z| \approx 1.4$ kpc due to a finite number of particles in each cell volume.

If the Aquarius group is a feature of a disc-satellite interaction, the perturber must have a mass on the order of a large globular cluster or a dSph satellite to produce the residual pattern in orbital energy and angular momenta. The Sagittarius dSph galaxy is an obvious candidate, but ω -Centauri is also a possible perturber. On the basis on position, velocities, chemical abundances and orbit, we identify C222531-145437 was highly likely stripped from ω -Centauri in the past. Thus, it is plausible that ω -Centauri has disrupted galactic stars as it passed through the plane, adding to any other oscillating modes rippling through the disc, resulting in what we now observe as the Aquarius stream.

7. CONCLUSIONS

We have presented a detailed chemical and dynamical analysis for 5 members of the recently discovered Aquarius stream from data taken with the MIKE spectrograph on the Magellan Clay telescope. Hereafter we solely refer to the discovery as a co-moving group instead of a stellar stream, as we find no evidence that the group is a tidal tail of a disrupted satellite. The main conclusions are as follows:

- The Aquarius stream is not mono-metallic. A wide spread in metallicities is observed, with $[Fe/H]$ ranging from -0.63 to -1.58 dex in just 5 members.
- No Na-O anti-correlation is observed in the Aquarius group. Two members have slightly enhanced levels of sodium with respect to iron. If the candidates were *known globular cluster members*, they would be classified as belonging to either the primordial component, or at most, tenuous membership could be argued for the lower envelope of the intermediate group.
- We find a strong positive Mg-Al relationship, reminiscent of Milky Way field stars and contrary to globular cluster observations.
- We find no evidence that the Aquarius group is the result of a disrupted classical globular cluster. The large $[Fe/H]$ variation severely limits the number of possible parent hosts, and both the extreme and intermediate component of the Na-O anti-correlation have not been observed. In total, high-resolution spectra exists for more than half of the stream.
- The co-moving group shows an α -enhancement of $[\alpha/Fe] = +0.40$ dex, similar to the Milky Way, and distinct to that typically observed in stars in dSph galaxies with comparable metallicities.

- Aquarius members are enhanced in [Na/Fe] and [Ni/Fe] to levels typically observed in either the thick disc or globular clusters. These levels of [Na/Fe] and [Ni/Fe] enhancement are not observed in stars from dSph galaxies. Low [Ba/Y] abundance ratios are also observed in the Aquarius group, in conflict with chemistry of present day dSph galaxies. Thus, on the basis of [(Na, Ni, α)/Fe] and [Ba/Y] abundance ratios, it is unlikely the Aquarius co-moving group is the result of a tidally disrupted dSph galaxy.
- One of our candidates, C222531-145437, has an abundance pattern that is clearly distinct from the other Aquarius members, most notably in barium where [Ba/Fe] = 0.68 dex. We exclude the possibility that the abundance variations have resulted from an AGB companion.
- The position and velocity C222531-145437 coincides precisely where simulations by Majewski et al. (2012) predict large amounts of ω -Centauri tidal debris, and the orbital energy and angular momenta are consistent with the ω -Centauri cluster. The chemical and phase-space information suggests that C222531-145437 is a rare tidal debris member of the globular cluster ω -Centauri. Removing C222531-145437 from the Aquarius sample does not extinguish or diminish any of the aforementioned conclusions.
- While no evidence exists for an accreted origin, and the Aquarius group members are indistinguishable from thick disc/halo stars, we hypothesise the co-moving group is the result from a disc-satellite interaction. We see no coherent pattern in the $U-V$ plane from Monte-Carlo simulations, but the orbital energies and angular momenta for the Aquarius group qualitatively reproduces patterns predicted by Gómez et al. (2012a). This is consistent with a minor merger in the Milky Way thick disc occurring perhaps up to a few gigayear ago. Given the location and velocity of the Aquarius group, and the identification of C222531-145437 as a star tidally stripped from ω -Centauri, it is plausible that the Milky Way- ω Cen interaction sufficiently perturbed outer disc/halo stars to produce what we now observe as the Aquarius group.

It is clear that not all co-moving groups are tidal tails of disrupted satellites, and that the structure of the Milky Way is indeed complex. While we find no chemical evidence that the Aquarius group is a tidal tail from a disrupted satellite, we propose the members are Galactic in origin, and the co-moving group is a result of a disc-satellite interaction. Thus, although the Aquarius group has not been accreted onto the galaxy, it certainly adds to the rich level of kinematic substructure within the Milky Way.

We are indebted to David Nidever and Steven Majewski for kindly replicating a plot from their ω -Centauri simulations (Figure 13 in this text) which helped to place C222531-145437 in context of the cluster's tidal

debris. A.R.C. acknowledges the financial support through the Australian Research Council Laureate Fellowship LF0992131, and from the Australian Prime Minister's Endeavour Award Research Fellowship, which facilitated his research at MIT. This publication makes use of data products from the Two Micron All Sky Survey, which is a joint project of the University of Massachusetts and the Infrared Processing and Analysis Center/California Institute of Technology, funded by the National Aeronautics and Space Administration and the National Science Foundation.

REFERENCES

- Allende Prieto, C., Lambert, D. L., & Asplund, M. 2001, ApJ, 556, L63
- Alonso, A., Arribas, S., & Martínez-Roger, C. 1999, A&AS, 140, 261
- Aoki, W., et al. 2007, ApJ, 660, 747
- Arnett, W. D., & Truran, J. W. 1969, ApJ, 157, 339
- Arnould, M., Goriely, S., & Jorissen, A. 1999, A&A, 347, 572
- Asplund, M., & García Pérez, A. E. 2001, A&A, 372, 601
- Asplund, M., Grevesse, N., Sauval, A. J., & Scott, P. 2009, ARA&A, 47, 481
- Barber, C., Dobkin, D., & Huhdanpaa, H. 1996, ACM Transactions on Mathematical Software (TOMS), 22, 469
- Baumüller, D., & Gehren, T. 1997, A&A, 325, 1088
- Bekki, K., & Freeman, K. C. 2003, MNRAS, 346, L11
- Bell, E. F., et al. 2008, ApJ, 680, 295
- Belokurov, V., et al. 2007, ApJ, 658, 337
- Bensby, T., Oey, M. S., Feltzing, S., & Gustafsson, B. 2007, ApJ, 655, L89
- Bergemann, M., Pickering, J. C., & Gehren, T. 2010, MNRAS, 401, 1334
- Bernstein, R., Shectman, S. A., Gunnels, S. M., Mochnicki, S., & Athey, A. E. 2003, in Society of Photo-Optical Instrumentation Engineers (SPIE) Conference Series, Vol. 4841, Society of Photo-Optical Instrumentation Engineers (SPIE) Conference Series, ed. M. Iye & A. F. M. Moorwood, 1694
- Bovy, J. 2010, ApJ, 725, 1676
- Bovy, J., & Hogg, D. W. 2010, ApJ, 717, 617
- Breddels, M. A., et al. 2010, A&A, 511, 90
- Brown, J. A., Smith, V. V., Lambert, D. L., Dutchover, Jr., E., Hinkle, K. H., & Johnson, H. R. 1990, AJ, 99, 1930
- Bullock, J. S., & Johnston, K. V. 2005, ApJ, 635, 931
- Burnett, B., & Binney, J. 2010, MNRAS, 407, 339
- Burris, D. L., Pilachowski, C. A., Armandroff, T. E., Sneden, C., Cowan, J. J., & Roe, H. 2000, ApJ, 544, 302
- Carretta, E., Lucatello, S., Gratton, R. G., Bragaglia, A., & D'Orazi, V. 2011, A&A, 533, A69
- Carretta, E., et al. 2009, A&A, 505, 117
- . 2010, A&A, 520, A95
- Casagrande, L., Ramírez, I., Meléndez, J., Bessell, M., & Asplund, M. 2010, A&A, 512, 54
- Castelli, F., & Kurucz, R. L. 2003, in IAU Symposium, Vol. 210, Modelling of Stellar Atmospheres, ed. N. Piskunov, W. W. Weiss, & D. F. Gray, 20
- Cayrel, R., et al. 2004, A&A, 416, 1117
- Cristallo, S., Straniero, O., Gallino, R., Piersanti, L., Domínguez, I., & Lederer, M. T. 2009, ApJ, 696, 797
- Da Costa, G. S., & Coleman, M. G. 2008, AJ, 136, 506
- Da Costa, G. S., Held, E. V., Saviane, I., & Gullieuszik, M. 2009, ApJ, 705, 1481
- De Silva, G. M., D'Orazi, V., Melo, C., Torres, C. A. O., Gieles, M., Quast, G. R., & Sterzik, M. 2013, MNRAS, 431, 1005
- Dehnen, W. 2000, AJ, 119, 800
- Dinescu, D. I. 2002, in Astronomical Society of the Pacific Conference Series, Vol. 265, Omega Centauri, A Unique Window into Astrophysics, ed. F. van Leeuwen, J. D. Hughes, & G. Piotto, 365
- Dotter, A., Chaboyer, B., Jevremović, D., Kostov, V., Baron, E., & Ferguson, J. W. 2008, ApJS, 178, 89
- Drake, A. J., et al. 2013, ApJ, 765, 154

- Francois, P., Spite, M., & Spite, F. 1988, *A&A*, 191, 267
- Frebel, A., Casey, A. R., Jacobson, H. R., & Yu, Q. 2013, *ApJ*, 769, 57
- Freeman, K., & Bland-Hawthorn, J. 2002, *ARA&A*, 40, 487
- Frischknecht, U., Hirschi, R., & Thielemann, F.-K. 2012, *A&A*, 538, 2
- Fulbright, J. P. 2000, *AJ*, 120, 1841
- Fux, R. 2001, *A&A*, 373, 511
- García Pérez, A. E., Asplund, M., Primas, F., Nissen, P. E., & Gustafsson, B. 2006, *A&A*, 451, 621
- Gómez, F. A., Minchev, I., O’Shea, B. W., Beers, T. C., Bullock, J. S., & Purcell, C. W. 2013, *MNRAS*, 429, 159
- Gómez, F. A., Minchev, I., Villalobos, Á., O’Shea, B. W., & Williams, M. E. K. 2012a, *MNRAS*, 419, 2163
- Gómez, F. A., et al. 2012b, *MNRAS*, 423, 3727
- Gratton, R. G., & Sneden, C. 1991, *A&A*, 241, 501
- Gratton, R. G., Sneden, C., Carretta, E., & Bragaglia, A. 2000, *A&A*, 354, 169
- Grevesse, N., & Sauval, A. J. 1998, *Space Sci. Rev.*, 85, 161
- Hansen, C. J., Bergemann, M., Cescutti, G., François, P., Arcones, A., Karakas, A. I., Lind, K., & Chiappini, C. 2013, *A&A*, 551, 57
- Helmi, A. 2008, *A&A Rev.*, 15, 145
- Helmi, A., & White, S. D. M. 1999, *MNRAS*, 307, 495
- Henden, A. A., Levine, S. E., Terrell, D., Smith, T. C., & Welch, D. 2012, *Journal of the American Association of Variable Star Observers (AAVSO)*, 40, 430
- Herwig, F. 2005, *ARA&A*, 43, 435
- Johnson, C. I., & Pilachowski, C. A. 2010, *ApJ*, 722, 1373
- Jurić, M., et al. 2008, *ApJ*, 673, 864
- Karakas, A., & Lattanzio, J. C. 2007, *Proc. Astron. Soc. Aust.*, 24, 103
- Karakas, A. I. 2010, *MNRAS*, 403, 1413
- Karakas, A. I., & Lattanzio, J. C. 2003, *Publications of the Astron. Soc. of Australia*, 20, 279
- Karakas, A. I., Lugaro, M. A., Wiescher, M., Görres, J., & Ugalde, C. 2006, *ApJ*, 643, 471
- Kirby, E. N., Lanfranchi, G. A., Simon, J. D., Cohen, J. G., & Guhathakurta, P. 2011, *ApJ*, 727, 78
- Kobayashi, C., Karakas, A. I., & Umeda, H. 2011, *MNRAS*, 414, 3231
- Kobayashi, C., & Nakasato, N. 2011, *ApJ*, 729, 16
- Lawler, J. E., Bonvallet, G., & Sneden, C. 2001, *ApJ*, 556, 452
- Lopez-Corredoira, M., Moitinho, A., Zaggia, S., Momany, Y., Carraro, G., Hammersley, P. L., Cabrera-Lavers, A., & Vazquez, R. A. 2012, “astro-ph:1207.2749”
- Majewski, S. R., Nidever, D. L., Smith, V. V., Damke, G. J., Kunkel, W. E., Patterson, R. J., Bizyaev, D., & García Pérez, A. E. 2012, *ApJ*, 747, L37
- Marino, A. F., Milone, A. P., Piotto, G., Villanova, S., Bedin, L. R., Bellini, A., & Renzini, A. 2009, *A&A*, 505, 1099
- Marino, A. F., et al. 2011, *A&A*, 532, 8
- Martin, N. F., Ibata, R. A., Bellazzini, M., Irwin, M. J., Lewis, G. F., & Dehnen, W. 2004, *MNRAS*, 348, 12
- Meyer, B. S. 1994, *ARA&A*, 32, 153
- Minchev, I., Quillen, A. C., Williams, M., Freeman, K. C., Nordhaus, J., Siebert, A., & Bienaymé, O. 2009, *MNRAS*, 396, L56
- Miyamoto, M., & Nagai, R. 1975, *PASJ*, 27, 533
- Momany, Y., Zaggia, S. R., Bonifacio, P., Piotto, G., De Angeli, F., Bedin, L. R., & Carraro, G. 2004, *A&A*, 421, L29
- Munari, U., Sordo, R., Castelli, F., & Zwitter, T. 2005, *A&A*, 442, 1127
- Navarro, J. F., Frenk, C. S., & White, S. D. M. 1997, *ApJ*, 490, 493
- Newberg, H. J., et al. 2002, *ApJ*, 569, 245
- Nissen, P. E., Chen, Y. Q., Schuster, W. J., & Zhao, G. 2000, *A&A*, 353, 722
- Nissen, P. E., & Schuster, W. J. 1997, *A&A*, 326, 751
- . 2010, *A&A*, 511, L10
- . 2011, *A&A*, 530, 15
- Nordström, B., et al. 2004, *A&A*, 418, 989
- Norris, J. E., & Da Costa, G. S. 1995, *ApJ*, 441, L81
- Norris, J. E., Ryan, S. G., & Beers, T. C. 1996, *ApJS*, 107, 391
- . 2001, *ApJ*, 561, 1034
- Plez, B., Masseron, T., & Van Eck, S. 2008, in *Cool Stars, Stellar Systems and the Sun*, ASP Conference Series
- Prantzos, N., Charbonnel, C., & Iliadis, C. 2007, *A&A*, 470, 179
- Purcell, C. W., Bullock, J. S., Tollerud, E. J., Rocha, M., & Chakrabarti, S. 2011, *Nature*, 477, 301
- Ramírez, I., & Meléndez, J. 2005, *ApJ*, 626, 465
- Reddy, B. E., Lambert, D. L., & Allende Prieto, C. 2006, *MNRAS*, 367, 1329
- Reddy, B. E., Tomkin, J., Lambert, D. L., & Allende Prieto, C. 2003, *MNRAS*, 340, 304
- Robin, A. C., Reylé, C., Derrière, S., & Picaud, S. 2003, *A&A*, 409, 523
- Roederer, I. U., Sneden, C., Thompson, I. B., Preston, G. W., & Shectman, S. A. 2010, *ApJ*, 711, 573
- Saviane, I., da Costa, G. S., Held, E. V., Sommariva, V., Gullieuszik, M., Barbuy, B., & Ortolani, S. 2012, *A&A*, 540, A27
- Schlegel, D. J., Finkbeiner, D. P., & Davis, M. 1998, *ApJ*, 500, 525
- Schönrich, R. 2012, *MNRAS*, 427, 274
- Sharma, S., Bland-Hawthorn, J., Johnston, K. V., & Binney, J. 2011, *ApJ*, 730, 3
- Shetrone, M. D. 1996, *AJ*, 112, 1517
- Siebert, A., et al. 2011, *AJ*, 141, 187
- Simmerer, J., Ivans, I. I., Filler, D., François, P., Charbonnel, C., Monier, R., & James, G. 2013, *ApJ*, 764, L7
- Skrutskie, M. F., et al. 2006, *AJ*, 131, 1163
- Smith, V. V., Suntzeff, N. B., Cunha, K., Gallino, R., Busso, M., Lambert, D. L., & Straniero, O. 2000, *AJ*, 119, 1239
- Sneden, C. A. 1973, PhD thesis, The University of Texas at Austin.
- Sobeck, J. S., et al. 2011, *AJ*, 141, 175
- Stanford, L. M., Da Costa, G. S., & Norris, J. E. 2010, *ApJ*, 714, 1001
- Steinmetz, M., et al. 2006, *AJ*, 132, 1645
- Travaglio, C., Gallino, R., Arnone, E., Cowan, J., Jordan, F., & Sneden, C. 2004, *ApJ*, 601, 864
- Tsuchiya, T., Dinescu, D. I., & Korchagin, V. I. 2003, *ApJ*, 589, L29
- Tsuchiya, T., Korchagin, V. I., & Dinescu, D. I. 2004, *MNRAS*, 350, 1141
- Uttenthaler, S., et al. 2011, *A&A*, 531, A88
- Van Eck, S., & Jorissen, A. 1999, *A&A*, 345, 127
- Venn, K. A., Irwin, M., Shetrone, M. D., Tout, C. A., Hill, V., & Tolstoy, E. 2004, *AJ*, 128, 1177
- Ventura, P., Carini, R., & D’Antona, F. 2011, *MNRAS*, 415, 3865
- Villalobos, Á., & Helmi, A. 2008, *MNRAS*, 391, 1806
- Widrow, L. M., Gardner, S., Yanny, B., Dodelson, S., & Chen, H.-Y. 2012, *ApJ*, 750, L41
- Williams, M. E. K., et al. 2011, *ApJ*, 728, 102
- Wylie-de Boer, E., Freeman, K., & Williams, M. 2010, *AJ*, 139, 636
- Wylie-de Boer, E., Freeman, K., Williams, M., Steinmetz, M., Munari, U., & Keller, S. 2012, *ApJ*, 755, 35
- Yong, D., Carney, B. W., & Teixera de Almeida, M. L. 2005, *AJ*, 130, 597
- Zwitter, T., et al. 2008, *AJ*, 136, 421
- . 2010, *A&A*, 522, A54